NTNU

Norwegian University of
Science and Technology

2-D and 2.5-D Multi-scale Full-Waveform Inversion in frequency domain for high-resolution P-wave velocity (Vp) and quality factor (Q) models at Sleipner field.

Henderson Gabriel Pinto Guerrero

Petroleum Geosciences
Submission date: November 2018
Supervisor: Børge Arntsen, IGP

Norwegian University of Science and Technology
Department of Geoscience and Petroleum

Acknowledgements

I would like to thank Anouar Romdhane for all the encouragement and wise words he gave me throughout the process. Being completely honest, I could not have done it without your help. I owe you a few ones...

To my sister, fly high!

Preface

This thesis is made as a completion of the master education in Petroleum Geophysics at Norwegian University of Science and Technology in Norway, 2018.

Abstract

In this work, we have applied a multi-scale discretized Full-Waveform Inversion in frequency-space domain considering both the 2-D and 3-D viscoacoustic wave equation for deriving P-wave velocity (Vp) and quality factor (Q) models in two inlines extracted from two vintages of the Sleipner Field (1994 and 2008).

The algorithm uses the waveform information from the pre-stack datasets of the Sleipner field recorded in 1994 and 2008 (before and after the injection of had CO_2 started). A pre-processing workflow, aiming to enhance the signal to noise ratio (S/N) without harming the amplitudes, is applied to the data before the application of the FWI method.

In a first stage, several tests were performed on synthetic data, aiming to measure the sensitivity of the algorithm when it comes to handle noisy sources, a less reliable initial model and different spacing grids. From these test, it was found that the algorithm is quite sensitive to handle noise in the sources, having converged to a local minimum when a S/N ratio below 5 is used. It was also found that a starting initial velocity model is critical to avoid cycle skipping and thus convergence to a local minimum. On the other hand, a bigger spacing grid can be used without losing critical information.

The impact of the initial model is also measured in the real dataset by performing a 2-D FWI. Where an improvement in the resolution of the P-wave velocity models were achieved by using a more accurate initial velocity for the Inline 1874 of the 2008 vintage.

A following test regarding the update of the density were performed, in which no sign of improvement was achieved by using the Gardner's equation to update the density, respect to the velocity. On the contrary, it added artifacts and increased the computational time of the inversion.

Two approaches were applied in order to asses the time-lapse difference of the vintages. A "cascade" approach is considered to give better indication of the lateral extension and change in velocity values due to the injection of CO_2 in the reservoir. However, the results obtained for both approaches bear zones with strong difference in velocity which is not expected to happen. This might be due to the limitation in iterations, different possible local minima for each data set in the "parallel approach" and the assumption that the baseline is fully inverted and its global minimum is achieved before it is used as initial model in the "cascade approach"

Attenuation has been considered by the relationship between the quality factor (Q) and the complex value of the velocity. Results from the attenuation inversion show a smooth behavior of the distribution of the parameter and a decrease in the zone where the gas is expected to be accumulated.

A last inversion consisted in a multiparameter FWI, inverting for both P-wave velocity and quality factor, where a strong "trade-off" between the parameters is shown in the results.

.

Preface

This thesis is made as a completion of the master education in Petroleum Geophysics at Norwegian University of Science and Technology in Norway, 2018.

Table of contents

List of Figures

Chapter 1

Introduction

Since the late 1960s, seismology has been applied to prospect the natural resources in the subsurface: a production-oriented branch of seismology that is often termed as exploration seismology (Sheriff and Geldart, 1995). Such branch relies on the study of the propagation of the seismic waves in the subsurface, a study in which the geoscientific community has spent decades of effort in an attempt to fully understand.

As a result of this effort, several imaging methods have been developed in the past years. These methods are commonly divided into two main categories. The first category consists of migration methods, aiming to image the the high-frequency structures of the subsurface. The second category, seismic inversion, consists of methods that estimate the physical properties of the subsurface through an inversion process.

As the seismic imaging methods require a velocity model,the velocity building step is critical and has a direct influence in the accuracy or success of the migration.

Regarding the building of the velocity models, among the most well-known techniques are: reflection traveltime tomography (Stork, 1992) and migration velocity analysis (Sava, 2004). Both approaches make approximations for modeling wave propagation such as the

high-frequency approximation or the one-way approximation of the wave equation. In the 80's, however, Lailly (1983), Tarantola (1984) and Mora (1987) suggested a new inversion strategy known as full-waveform inversion (FWI). By iteratively minimizing the misfit between observed and modeled seismograms, this technique uses the full information content given by the waveforms, deriving velocity models of a higher resolution than those provided by the conventional methods. These improved velocity models can help to derive migrated images with higher resolution and better reflector positioning, as it is discussed in Vigh et al. (2010).

1.1 FWI and the local gradient method

As stated above, the full-waveform inversion uses the full information content given in the waveforms and can consequently offer a much better-resolved image of the 3D subsurface structures. It basically consist of minimizing the misfit between the observed and the modelled data, aiming to determine the optimal model, which could explains the observed data in a better way.

The straightforward way would be to apply a global search, like the Monte Carlo approach to find the global misfit minimum. However, this is computationally accomplishable only for a very limited set of model parameters and thus not suited for the general multiparameter model (Operto et al., 2013). To overcome this computational limitation, the most widely used optimization methods are gradient-based algorithms. In general, these methods search for a minimum of the misfit function in the vicinity of the starting model. However, the seismic inverse problem is generally highly nonlinear and the misfit function is not smooth, but characterized by local minima (Figure 1.1). Consequently. the local inversion method bears the danger to end up in one of the local minima, which is a major problem in FWI. Requiring a sufficiently accurate starting model for a successful inversion.

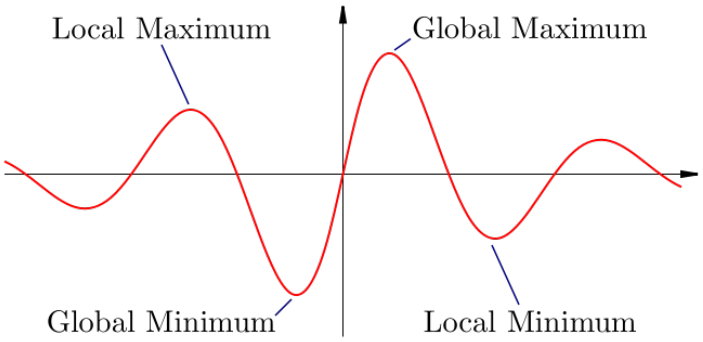

Figure 1.1: Distinction between local and global extreme values of a function.

Among the optimization methods the most sophisticated is the class of Newton methods which take the full Hessian, the second derivative of the misfit function, into account. They lead to a better convergence and can result in improved subsurface images (Virieux and Operto, 2009). Still, the high computational costs make them unattractive for large inverse problems (Pratt, 1999). Alternatives are quasi-Newton algorithms. It estimates the Hessian from changes in the misfit gradient and can, therefore, be implemented at lower computational costs. Another method successfully applied in FWI is the truncated Newton method, which approximates the Hessian by the second-order adjoint formula (Metivier. et al., 2017). The adjoint method was originally formulated in the time domain by Tarantola (1984) and then developed by Pratt (1990b).

1.2 Frequency vs Time

Even though it remains unclear, which approach (time or frequency domain) is the most efficient one for full-waveform inversion. The final decision might rely on the characteristics of the study such as acquisition geometry or frequency content. In this study we have implemented an FWI in the frequency domain, which presents some distinct advantages with respect to the time-domain formulation, (Pratt (1990a); Pratt (1999) and Sirgue and Pratt (2004)) such as:

1. Contrary to time domain approach, the frequency domain FWI is generally carried out by successive inversions of single frequencies or packs of a few discrete frequencies . The simulations cover from the lowest to the highest frequencies, a framework that is usually called "multi-scale inversion" (Bunks et al., 1995) and it might mitigate the non-convergence of the inverse problem associated with high-frequency cycle-skipping

2. The redundancy of aperture angle on the wavenumber illumination of the multifold surveys can be decimated in order to apply more efficient numerical approaches than those applied in the time domain FWI. Resulting in fewer inversions to perform in order to build a reliable velocity model.

3. Attenuation can be implemented in the forward problem in a straightforward way, and without extra computational cost, by using complex velocities (Song et al., 1995).

1.2.1 Multi-scale inversion in frequency domain

As mentioned above, the seismic inverse problem is highly nonlinear and requires an iterative approach to fit the modelled and observed data (Tarantola, 1984). Moreover, as a local inversion method, FWI is prone to end up in one of the numerous local minima of the objective function (Figure 1.1.)

In an attempt to solve this problem, multi-scale decomposition of the seismic inversion had been proposed. Accordingly to Bunks et al. (1995), at long scales, the number of local minima is greatly reduced and those minima that remain are further apart from each other (Figure 3.3).

In other words, the FWI can be implemented at a long scale of the problem, with higher possibilities of finding the global minimum of the problem or at least a local minimum that is in the near neighborhood of the global minimum. This solution of the inverse problem is

then fined-up for successively shorter scales.

1.3 Visco-Acoustic wave equation

Depending on the problem, it is common to use certain approximations of the wave equation. A main area of FWI application is the marine environment. In these scenarios, the wave propagation is mainly approximated using the acoustic or visco-acoustic wave equation. Which only considers compressional waves. For land seismic, the abundance of prominent shear waves and surface waves favors an inversion, involving the according parameters, such as compressional-wave velocity, shear-wave velocity and density. Depending on the subsurface, anisotropic parameters might need to be included. Still, these parameter classes are very challenging to invert for (Virieux and Operto, 2009) and are often integrated only as passive parameters in the forward simulation.

In this study, we have considered the visco-acoustic wave equation to be solved. This simplification in the subsurface description results from three main reasons:

1. The first one is computational related. Solving the elastic wave equation is generally 2-3 orders of magnitude more computationally intensive than the acoustic wave equation due to the extra wavefield components needed to be computed.

2. The second one is ill-posedness problem nature related. The misfit function has several local minima, mainly due to lack of low frequencies, acquisition problems or inaccuracy of the initial model. By considering elastic wave equation, several parameters have to be added, implying more unknowns to the problem.

3. As stated above, due to the frequency domain approach considered in the inversion, the implementation of the attenuation, can be achieved without great efforts, based

on the use of complex velocities within the visco-acoustic equation. In the inversion framework applied, the attenuation is considered following the Kolsky-Futerman model (Kolsky (1956) and Futterman (1962).

By considering P-wave velocity and attenuation the FWI becomes a multi-parameter inversion, aiming to describe or characterize the subsurface in a more accurate. However, it is not that simple, since the parameters considered can have coupled effects, a phenomenon termed as "trade-off" (Butzer, 2015).

1.4 2D and 2.5D

In this work, we have considered 2D and 2.5D Full-waveform inversion schemes. Due to the associated computational cost for the applicability of full 3D FWI to our dataset, we propose a 2.5D inversion scheme, in which the solution of the full 3D visco-acoustic waveform is solved but only 5 planes in the Y space direction are considered. Two main advantages can be drawn from considering a 2.5D inversion:

1. In a 2D FWI scheme the dataset must be scaled prior to the inversion (Pratt, 1999), leading to possible artifacts into the parameters considered. In a 2.5D scheme, even though only 5 planes are considered, the dataset is not scaled prior the inversion and the solution of the full 3D visco-acoustic wave equation might improve the modelling of the geometrical spreading factor in comparison to the 2D scheme.

2. Another advantage might be linked to a better resolution of the crossline plane by a better treatment of the events in the inline plane.

1.5 Time-lapse FWI

The multi-scale apporach, such as the one consider in this work, can be adapted to resolve low or high wavenumber features of the subsurface. Making FWI a suitable option for inverting for time-lapse changes in the subsurface. Moreover, the technique can be apply to monitor a reservoir while producing, or to monitor the distribution of the injected CO_2 in a sequestration project.

In the last decade, several time-lapse FWI applications have been studied (Watanabe et al., 2004; Denli and Huang, 2009; Plessix et al., 2010; Zheng et al., 2011; Asnaashari et al. 2012; Routh et al., 2012; Queisser and Singh, 2013; Raknes and Arntsen, 2014; among others). However, application on real data is quite limited.

The main drawbacks of the time-lapse FWI method, are linked to the sensibility to repeatability problems, due to the difference in acquisition geometries, and numerical artifacts that may impact in a negative way, the inverted difference of the vintages.

In the last decade, time-lapse FWI have been mainly carried out following three different approaches:

1. Parallel approach: Separately inverting the baselin and monitoron a common initial model and then substract the results for comparison.

2. Cascade approach: Inverting them in a sequential way, in which the final model from the baseline inversion is used as starting model for the monitor inversion

3. Double-difference approach: with a baseline model inversion followed by a monitor inversion that solves the following optimization problem Recently, a relatively similar approach where, in addition, the observed dataset is slightly modified by adding the observed data residuals to the synthetic data from the first inversion, was developed

(Zheng et al., 2011) attempt to introduce into the inversion some degree of 4D coupling between vintages

In this work, we have applied the first two approaches to our datasets

The 4D FWI results using real timelapse Grane PRM data acquired in the field with a six-month acquisition interval between vintages show changes at the reservoir level that correlate with both injecting and producing wells

1.6 FWI as CO_2 monitoring tool for Sleipner Field

The injection of carbon dioxide (CO_2) into deep saline aquifers is one of three main options for the geological storage of CO_2 in order to decrease anthropogenic greenhouse gas emissions into the atmosphere. Previous studies have shown that compared to the other two major options (storage in depleted hydrocarbon reservoirs and in deep, un-mineable coal seams), deep saline aquifers have the highest potential capacity globally for CO_2 storage (Bachu, 2003). This attribute has been the driven force in the development of more than 10 saline aquifer injection projects over the last 10 years (Nordbotten et al., 2005).

The first project of this kind was launched in 1996 at the Sleipner gas field (Figure 2.1) in the Norwegian North Sea. Due to the high content of CO_2 associated to the gas (approximately 9%), Statoil decided to capture and store this CO_2 into the highly porous saline aquifer Utsira Fm, aiming to meet the sales gas requirements and avoid pollution to the atmosphere (Furre et al., 2017). The Utsira Fm is a high porosity and permeable sandstone at a depth between 800 and 1100 meters found at the Sleipner field. The CO_2 injection commenced through injection well 15/9-A-16 on September 15th 1996, since then, more than 16 Mt of CO_2 have been stored in the Utsira Sand (Hansen et al., 2005)

However, as in any CCS project, leakage of CO_2 out of the reservoir is a big concern.

Such migration out of the injection formation can lead to contamination of other subsurface resources, including groundwater resources in shallower formations (Little and Jackson, 2010). In order to demonstrate that the storage site is performing as predicted, a monitor portfolio has been established for Sleipner, with monitor techniques such as: Gravity surveys, CSEM or 3-D Seismic acquisitions. For the latter, several time lapse seismic surveys have been carried out in 1999, 2001, 2002, 2004, 2006, 2008, 2010, 2013 and 2016 (Furre et al., 2017).

The high quality of this time-lapse dataset has been used for scientists to developing and testing new inversion schemes, both inverting from seismic amplitudes to impedances, and further to rock physics properties. The data has been used for full, partial, and pre-stack 2D and 3D inversions, and in later years also Full Waveform Inversion (FWI).

Regarding CO_2 monitoring the strength of the FWI is the ability to characterize velocity changes induced by the CO_2 injection and accurately locate the plume due to the CO_2 migration. When entering the reservoir, the CO2 is normally in supercritical state. This provides a strong sonic velocity contrast to the initially brine filled reservoir. A velocity contrast that is exploted by the FWI.

In this work, we have used two data sets: 1) from a "baseline" survey from 1994 (acquired before the injection of the CO_2) and 2) from a "monitor" survey acquired in 2008 (12 years after the injection had started). With the objective of visualizing the plume development in terms of velocity changes.

1.7 Organization of the work

Chapter 2 will start with the description of the geological area and acquisition setting for the considered surveys for the real case study. Chapter 3 gives an overview of the visco-

acoustic wave equation propagation and the attenuation model considered. The concept of FWI and local optimization methods are introduced. The implementation and the main advantages of this frequency approach are discussed. Followed by the frequency selection technique applied and the pre-processing sequence. Chapter 4 presents the methodology and results of the implementation of the theoretical aspects discussed in chapter 3. In a first stage, the FWI is applied in the frequency domain to a 2-D synthetic case representing the Sleipner field. Afterwards, a multi-scale monoparameter full-waveform inversion is applied in 2-D domain to the data sets, termed as “baseline” and “monitor”. For both data sets, P-wave velocity (Vp) and attenuation (by quality factor Q) are inverted separately, with the update of the density given by the Gardner’s relationship. Followed by a multi-scale multiparameter inversion of both Vp and Q in a "simultaneous" and a "sequential" approach. A FWI is then applied to a 2.5D model for both datasets for Vp and Q. Finally, chapter 5 gives a summary and conclusion of the thesis

Chapter 2

Geological Setting

Being the first CO_2 sequestration project at big scale, there is plenty of information available regarding the properties of the field and the storage site. As mentioned before, the Sleipner Carbon Capture and Storage project started as a CO_2 sequestration project with the source of this greenhouse being its own hydrocarbon production from the Sleipner West gas field (Zweigel et al., 2004) (Figure 2.1) .

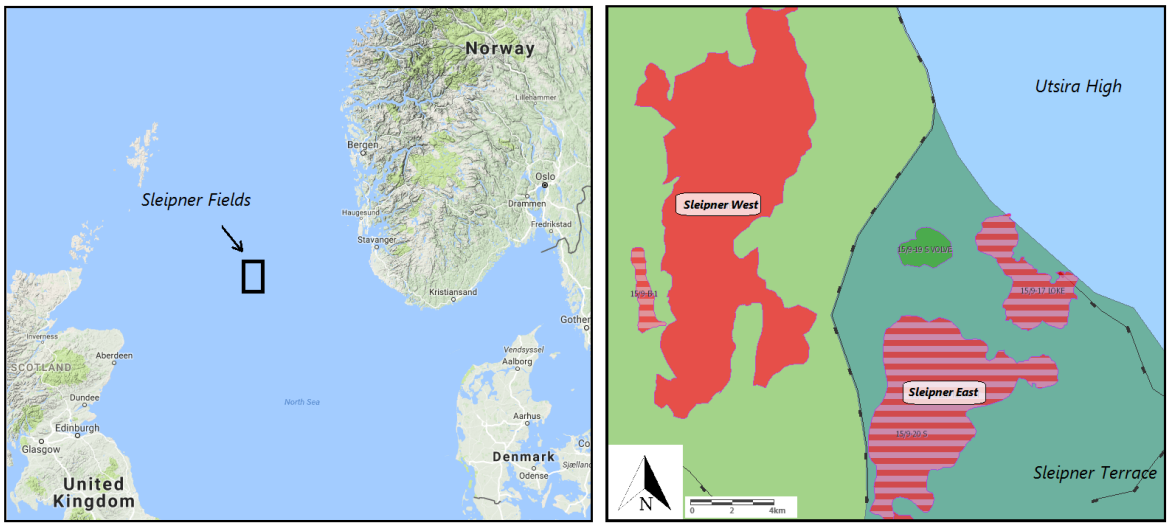

Figure 2.1: Left: location map. Right: the Sleipner fields (base maps courtesy of NPD).

The project begun in 1996, with an injection rate of 1 Mt/year with more than 16 Mt of CO2 injected so far. Before injection, CO2 is compressed to its dense supercritical state. At

this supercritical stage, the relatively high density difference between the formation fluids and the CO2 leads to strong buoyancy forces and provides a strong sonic velocity contrast to the initially brine filled reservoir and favourable conditions for seismic monitoring.

2.1 Utsira formation

Several studies have confirmed that the injected CO2 is safely trapped within the Utsira Fm with no leakage into the overburden to date (Chadwick et al. (2006); Arts and Eiken (2004); Furre et al. (2015))

The Utsira formation of the Nordland Group is a late Cenozoic post-rift succession of the North Sea, with an extension of more than 26000km2 (Holloway et al., 2000). The sands of the Utsira Fm display a complex architecture and the elongated sand body extends some 450 km N-S and 90 km E-W (Figure 2.2). It is formed by basically two depocentres. The southern depocentre is where the CO2 has been injected to, with a depth range from 800m to 1100m and an average thickness of 250m.

Holloway et al. (2000); give a very detailed geological description of the Utsira sand reservoir and caprocks, presenting results from a core data analysis concluding that the Utsira Sand sediments are mostly uncemented, fine to medium-grained sand, with occasional coarse grained beds. With a well leg response as a blocky pattern, low gamma ray and resistivity values.

The storage capacity of the Utsira Sand has been predicted at over 30 Gt (Zweigel et al., 2004), this high value is mainly due to its porosity and permeability properties, ranging from 27% to 30% and from 1 to 3 Darcy respectively (Chadwick et al., 2006). Within the storage reservoir, several thin shale layers, up to 1-2m thick, are also identified from wireline log data with high gamma ray values, considered as horizontal permeability seals for the

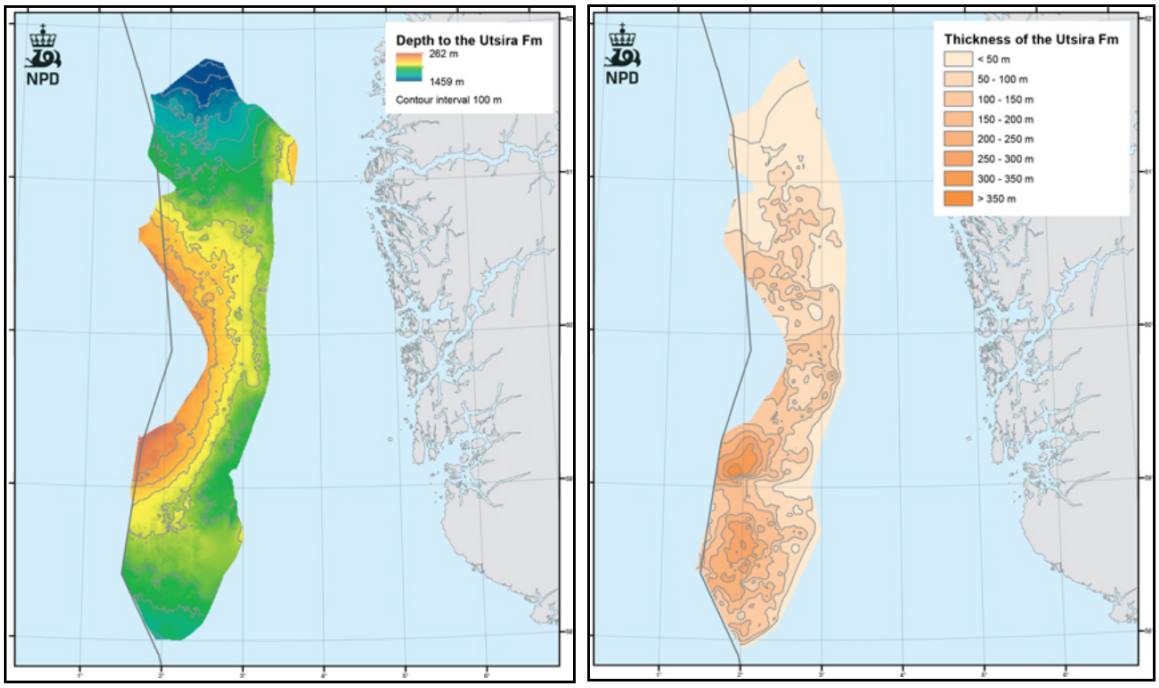

Figure 2.2: Left: Map view of the top of the Utsira Fm. Right: Thickness of the Utsira Fm. (Both maps courtesy of NPD).

CO2 (Chadwick et al., 2006). Furthermore, no faults have been reported from within the Utsira Sand, except for a few polygonal reverse faults penetrating the very lowermost part of reservoir, initiating from the Hordaland shales beneath (Zweigel et al., 2004).

Its top varies in depth from 250 to 1500m (Figure 2.2), showing a general dip towards the South. Near the Sleipner field, it is found mainly around a depth of 800 and 1100m (Chadwick et al., 2006). In contrast, the base of the formation presents an abrupt change of the gamma ray values decreasing upwards. This trend indicates the separation between the sand body and the underlaying shales of the Hordaland Group (Chadwick et al., 2006).

The thickness of the Utsira formation varies along with the depression of its base. Its range goes from 180 meters to 320 meters (Figure 2.2).

2.1.1 Caprocks

The Hordaland group represents the underlying unit to the Utsira reservoir (Figure 2.3). The group is mainly characterized by shales from the late Oligocene.

Meanwhile, the caprock to the Utsira Fm is formed by the Nordland Group (Figure 2.3). This is a hundreds-meters thick cap-rock shale from the lower and upper Pliocene. The caprock shale or the Nordland shale, comprises dominantly kaolinite, illite, quartz, and smectite. Based on the cutting analysis, that the caprock is assumed to be a good quality seal with a low probability of leakage (Chadwick et al., 2006)

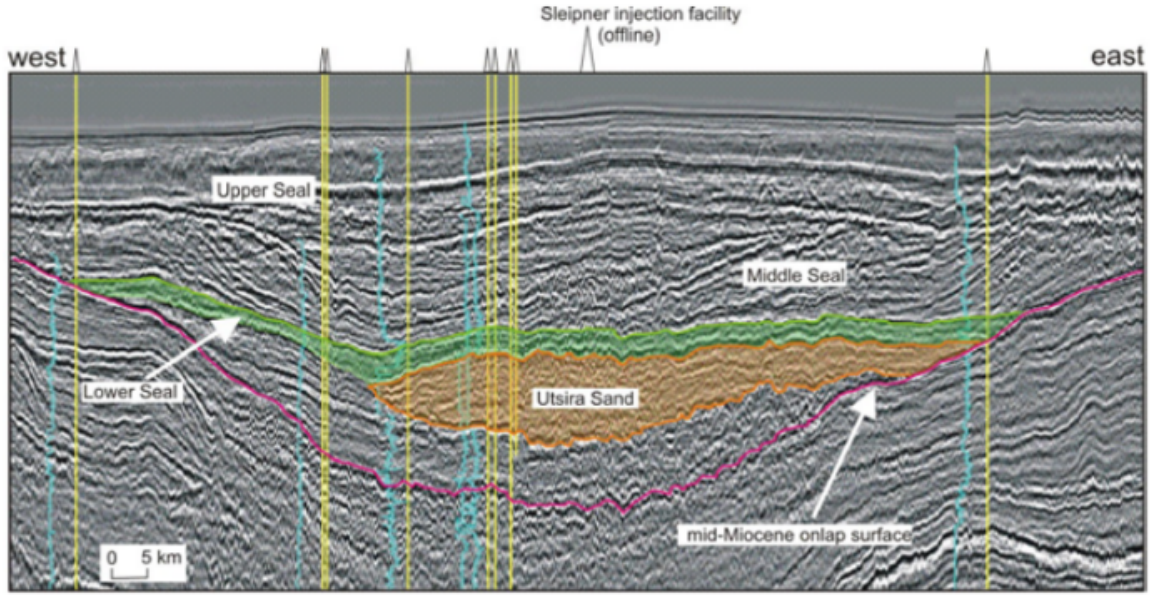

Figure 2.3: Left: Seismic section illustrating the Utsira Sand reservoir, its caprock and the underlying units. The 250 m thick Utsira Sand Formation is overlained by the Nordland shales, forming the Lower, Middle and Upper seals. (Taken from Chadwick et al. (2004)).

Figure 2.3 shows the geological structure of the Utsira Sand, which is surrounded by the Nordland shale on the top and the Hordaland shale on the bottom.

The main seal is subdivided in three sections according to (Arts and Eiken, 2004)

- The Lower seal (lower-upper Miocene): Is the shale overlaying the Utsira sandstone

with a thickness of up to 100m thickness (Holloway et al., 2000).

- The Middle seal(middle-uppder Miocene): Overlying The Lower seal and composed by sediments ranging from very fine to coarse, with a thickness between 100 and 170 meters.
- The Upper seal (upper Pliocene): The shallowest of the seals conformed mostly by shales.

.

Chapter 3

Full Wave Inversion Theory

In this chapter the theory behind the Full-Waveform Inversion (FWI) is introduced. Starting with a short description of the forward and inverse modelling problem in a general sense, followed by the introduction of the seismic inverse problem in FWI.

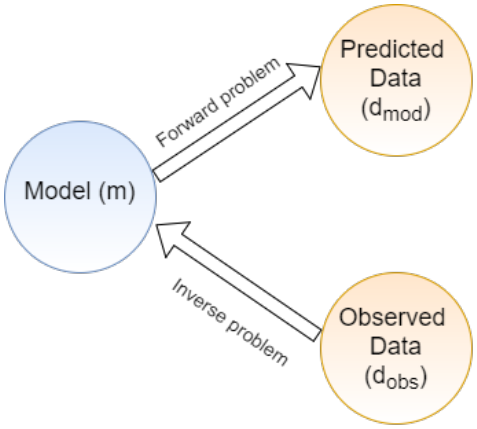

Figure 3.1: Sketch of the relationship between the Model and Data within the forward and inverse approach.

Numerical modeling of geophysical data for a given model parameter is often referred to as a forward problem (see Figure 3.1). The solution to the forward problem enables us to predict geophysical data from specific geological structures. In order to solve this problem,

a relationship between the model and the data has to be establish:

$$\vec{d} = G\vec{m} \tag{3.1}$$

Where:

$\vec{d}$: is the wavefield

$\vec{m}$: is the model

G : is the known relationship between the wavefield and the model

On the other hand, many studies aim to determine geological structures from geophysical data. Due to the complex internal structure of the earth, this kind of studies are ill-posed problems. Usually we use a more or less simple model to approximate the true geology and try to determine the model parameters from the data. We call this problem an inverse problem (see figure 3.1). The success of geophysical interpretation depends on whether or not we can approximate the true geological structure through a reasonable model and effectively solve the corresponding inverse problems.

The inverse problem can be formulated as:

$$\vec{m} = g^{-1}\vec{d} \tag{3.2}$$

Where:

$\vec{d}$: is the wavefield

$\vec{m}$: is the model

g^{-1} : is the inverse (when possible) of the relationship between the wavefield and the model

3.1 Frequency Domain Forward Modelling

So far, many strategies and computational schemes have been developed to make FWI a more practical and suitable technique. From different approaches for solving the forward problem (i.e. finite-difference methods, finite-element methods, finite-volume methods

among others) to different domain parametrization (i.e. time, frequency or Laplace-Fourier domains) (Virieux and Operto, 2009). In this work, a forward problem is applied to solve the visco acoustic wave equation in the frequency-space domain which can be written in 3D as:

$$\left[\frac{\omega^2}{\kappa(x,y,z)} + \frac{1}{\xi_x(x)}\frac{\partial}{\partial x}\frac{b(x,y,z)}{\xi_x(x)}\frac{\partial}{\partial x} + \frac{1}{\xi_y(y)}\frac{\partial}{\partial y}\frac{b(x,y,z)}{\xi_y(y)}\frac{\partial}{\partial y} + \frac{1}{\xi_z(z)}\frac{\partial}{\partial z}\frac{b(x,y,z)}{\xi_z(z)}\frac{\partial}{\partial z}\right]\mathcal{U}(x,y,z,\omega) = -f\,(x,y,z,\omega)$$

Or in a matrix formalism for each frequency in study:

$$(\mathbf{S})\mathbf{u} = -\mathbf{f} \qquad \text{where :} \quad \begin{array}{l} \mathbf{S} : \text{denotes the complex impedance matrix} \\ \mathbf{u} : \text{is the wavefield vector, pressure in our case} \\ \mathbf{f} : \text{is the source term} \end{array} \tag{3.3}$$

The solution to eq. 3.3 is efficiently obtained by LU decomposition of the system impedance matrix followed by forward and backward substitution. Once the modelled data dmod is obtained with the forward modeling, the data residuals are computed by:

$$\Delta\mathbf{d} = \mathbf{d_{mod}} - \mathbf{d_{obs}}; \qquad \text{for} \quad i = (1,2,3,...n) \tag{3.4}$$

with n equals the number of observations.

3.2 Inversion Modelling

A frequency-space domain formulation of the back-propagation gradient method of Lailly (1983) and Tarantola (1984) is reformulated in a matrix sense, following the work of Pratt et al. (1998).

Once the residuals are calculated as shown above (eq. 3.4), the objective function to minimize (also termed as cost function or misfit function) is the data residuals in a least-square sense, given by:

$$E(\mathbf{m}) = \tfrac{1}{2}\|\mathbf{d_{mod}} - \mathbf{d_{obs}}\|_2 \tag{3.5}$$

The optimization problem is solved with a gradient method, with equation given by:

$$\frac{\partial \mathbf{E(m)}}{\partial \mathbf{m}} = \Re e\{\mathbf{J}^t \delta \mathbf{d}^*\} \qquad \begin{aligned} &\mathbf{J}^t \text{ : is the transpose of the jacobian matrix.} \\ \text{where : } &\delta\mathbf{d}^* \text{ : is the complex conjugate of the data residuals} \\ &\Re e \text{ : denotes the real part of a complex number} \end{aligned} \tag{3.6}$$

In its most basic form, the gradient method provides the following relationship between the perturbation model at iteration n and the gradient of the misfit function:

$$\mathbf{m_{n+1}} = \mathbf{m_n} + \delta \mathbf{m_n}; \tag{3.7}$$

$$\delta \mathbf{m_n} = -\alpha \frac{\partial \mathbf{E(m)}}{\partial \mathbf{m}}; \tag{3.8}$$

The gradient of the misfit function represents the direction in which it increases fastest. Therefore, as we are trying to minimize the problem, the direction should be towards the opposite of the gradient (negative) (eq 3.8). The step length α is a positive scalar with the objective of converting the units of the gradient vector to model dimensions (Hicks and Pratt, 2001).

The J^t term in eq. 3.6 is the transpose of the Fréchet derivative matrix, which elements are given by:

$$J_{ij} = \frac{\partial u_i}{\partial m_j} \quad \text{for} \quad i = (1, 2, 3, ...n); \quad j = (1, 2, 3, ...m) \tag{3.9}$$

Where u and m, represent the seismic wavefield and the model parameters respectively. The explicit computation of the Jacobian matrix (Fréchet derivative matrix) would require m forward-propagation problems to be solved. This is extremely expensive in a computational sense. An analogous method to the back-propagation method applied by Tarantola (1984) and Pratt et al. (1998), and others is then applied to compute the gradient, using:

$$\mathbf{u} = \mathbf{S^{-1}f} \tag{3.10}$$

with **S**, the impedance matrix and **F** the virtual sources (see Pratt et al. (1998) for more details). Substituting 3.10 in 3.6 and 3.8 gives:

$$\delta\mathbf{m} = -\alpha\Re e\{\mathbf{f^t}[\mathbf{S^{-1}}]^\mathbf{t}\delta\mathbf{d}^*\} \quad \text{defining} \quad \mathbf{v} = [\mathbf{S^{-1}}]^\mathbf{t}\delta\mathbf{d}^*) \tag{3.11}$$

Where **v** is the analogous to the "backpropagated" residuals in time and is computed by solving a forward modeling problem with the source terms replaced by the conjugate residuals (Pratt et al., 1998).

The gradient is then computed by multiplying the (back propagated) residuals field **v** and the virtual sources **f**, (forward propagate field). This step is equivalent to the result of Tarantola (1984) in which the data residuals is propagated in reverse time and the time equivalents of **f** and **v** are zero-lag crosscorrelated. This result is closely related to most of the pre-stack depth migration algorithms (Hicks and Pratt, 2001).

According to Pratt (1999), the gradient method can be improved and give a better estimate by preconditioning or filtering by the inverse of the approximate Hessian. This precondition can also yield improved convergence rates and sharpens the gradient vector. The

approximate Hessian represents the second derivative matrix of the cost function respect the model parameters, the elements of which are given by:

$$diagH_a = diag\big(\Re e\{\mathbf{J^t J^*}\}\big) \tag{3.12}$$

Moreover, the algorithm applies a damping term (λ) to the Hessian before invert it. This term is known as the Levenberg-Marquardt damping parameter. Which is a dynamic value defined by:

$$\lambda = \lambda_0 \frac{E(i)}{||d_obs||} \tag{3.13}$$

with λ_0 the starting value of the damping parameter, $E(i)$ is the value of the misfit function at iteration i, which is divided by the L^2 norm of the observed value (Helgesen and Landrø, 1993). This factor is applied as a regularization factor to improve stability (Romdhane et al. 2014 Romdhane et al. (2014)).

The final iterative gradient method is then given by:

$$\delta m = -\alpha\big(diagH_a + \lambda I\big)^{-1}\nabla_m E \tag{3.14}$$

A summary of the whole iterative inversion process is given in Figure 3.2.

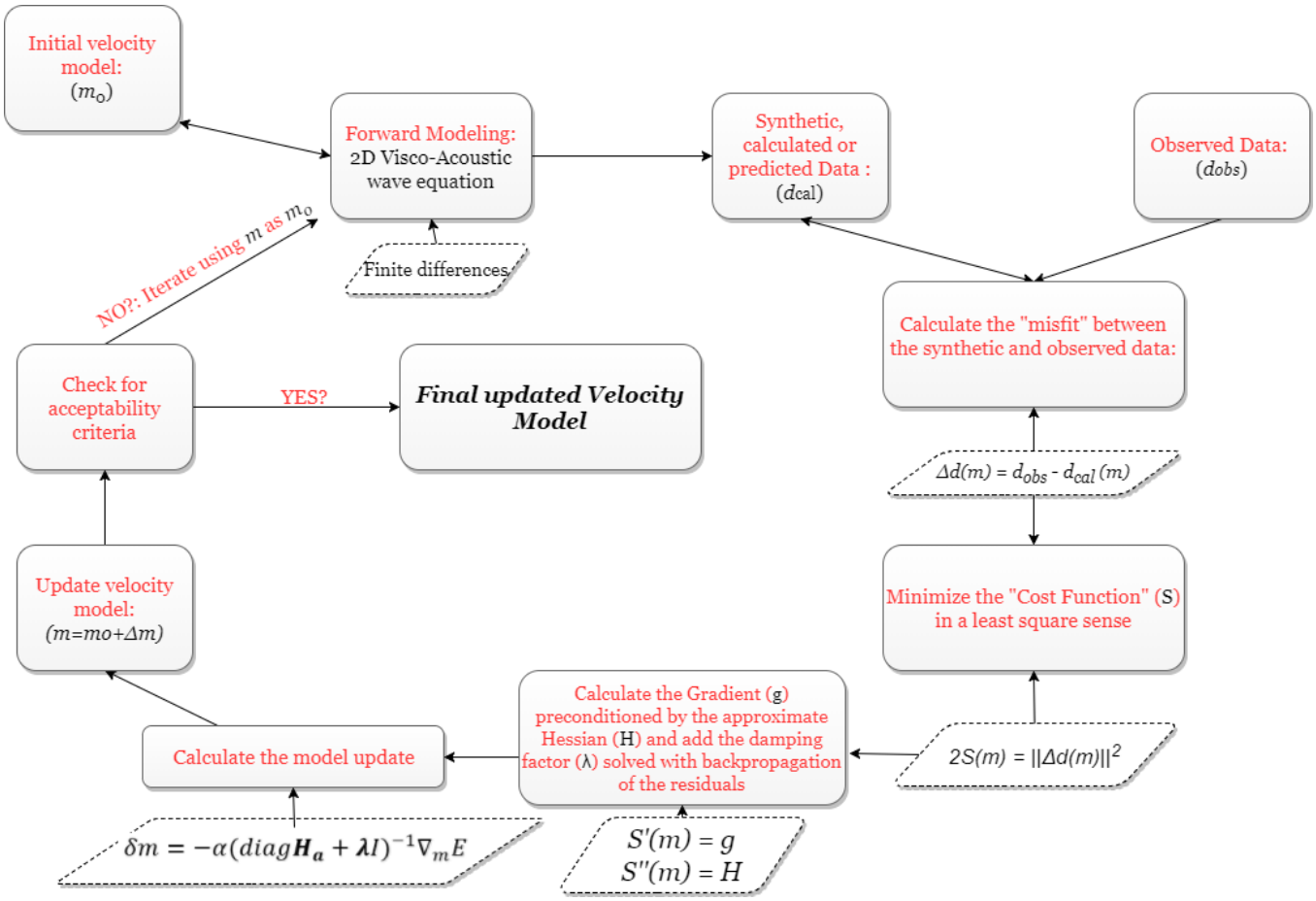

Figure 3.2: Workflow of the iterative Full waveform inversion algorithm developed by Romdhane et al. (2014).

3.3 Discrete frequency-domain inversion

Figure 3.2 illustrates the different steps to estimate the model update in one iteration. As explained before, a multi-scale apporach have been perform in order to avoid cycle-skipping problem and improve the computational cost (section 1.2.1). This approach is illustrated in Figure 3.3 from Bunks et al. (1995).

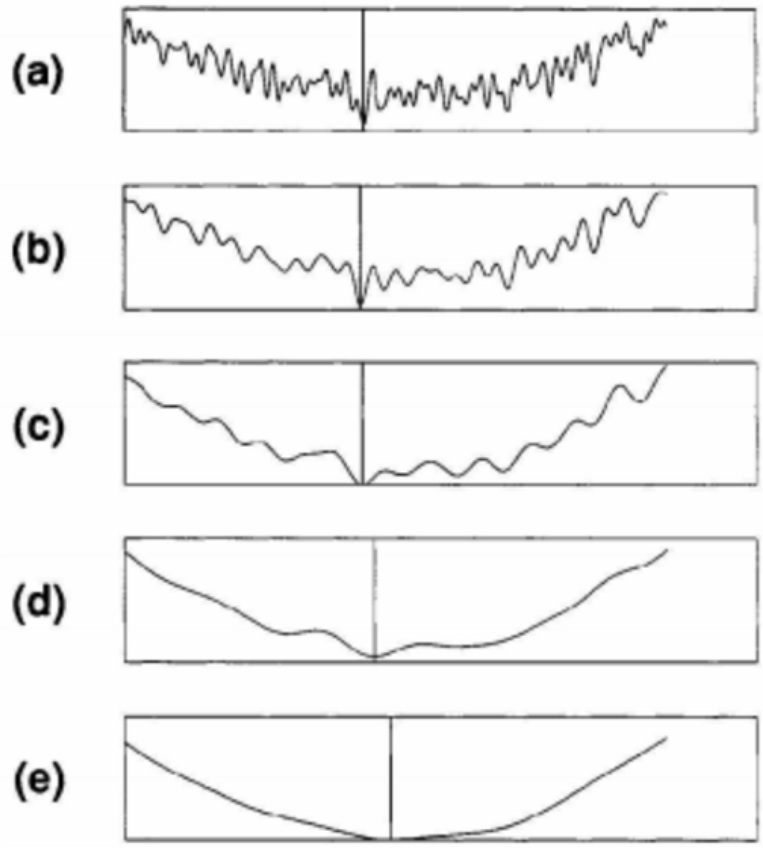

Figure 3.3: Illustration of an objective function decomposed onto 5 scale lengths, decreasing from (e) to (a). (Taken from: Bunks et al. (1995)).

The figure shows an objective function and its decomposition in four scales. The longest scale component of the problem, shown in Figure 3.3e, contains a single minimum and a smooth shape that could facilitate the finding of the global minimum. In this work, the multi-scale approach is divided into different frequency stages. Being the long scale represented by the lowest frequencies in our data.

After a global minimum has been found for the long scale, this is considered as our initial guess in a shorter scale (represented by higher frequencies in our case). This could increase the probabilities of finding the global minimum at the shorter scale due to the fact that the global minimum at the larger scale (Figure 3.3e) is in the vecinity of the global minimum in the shorter scale (Figure 3.3d). The step is performed again, creating an iterative process, with the objective of finding the global minimum of the original and finer scale problem (Figure 3.3a).

This technique not only contributes to the mitigation of the cycle-skipping problem but also improve the process, computationally speaking. After finding the global minimum at the larger scale or at least a near local minimum, less iterations are needed to refine the solution at the next scale since the solution obtained in the previous scale is in the vecinity of the new global minimum (Figure 3.3)

Two factors are critical in the success of the technique:

1. Low frequencies are critical in order to obtain an scale sufficiently convex so that the global minimum can be found easily

2. The initial model in which our FWI is based, have an implication on where our initial guess in the objective function would be. The less accurate the initial model, the further the initial guess from the global minimum.

Furthermore, Sirgue and Pratt (2004) showed that the choice of the frequencies needs to provide a continuous coverage of the wavenumber spectra and this can be fulfilled by estimating the frequencies by:

$$f_{n+1} = \frac{f_n}{\alpha_{min}} \tag{3.15}$$

with

$$\alpha_{min} = \frac{1}{\sqrt{1+{R_{max}}^2}} \tag{3.16}$$

where ${R_{max}}^2 = {h_{max}}/{z}$ is the half offset-to-depth ratio, resulting from considering the maximum half offset h_{max} and a particular depth z. From this, we can notice that α_{min} is smaller for larger maximum offsets. Therefore, the larger the maximum offsets available, the fewer the frequencies are required to fulfill the continuous coverage of the wavenumber spectra (Sirgue & Pratt, 2004).

We have decided to create groups of frequencies of only one frequency per group, what Brossier et al. (2009) have defined as the Bunks approach. Consisting in successive inversions of one-single frequency groups. The first group contains the starting frequency and one higher frequency is added from one group to the next.

The main drawback of the discrete frequency domain inversion is the loss of redundancy compared to time-domain FWI which can lead to problems in case of highly nonlinear problems such as surface waves (Virieux and Operto, 2009). Of course, this can be mitigated by using a denser frequency sampling. However for high numbers of frequencies per iteration, the storage space increases and the higher number of discrete Fourier transformations slows the inversion down. Thus, the time-frequency method becomes less efficient.

3.4 Attenuation and multiparameter inversion

Seismic attenuation has an important impact in the absorption of the wave energy and the dispersion distortion for the phase of the waves. Resulting in a consequent important impact on the FWI inversion result (Hicks and Pratt, 2001).

Waveform inversion of attenuation parameters was first formulated by Tarantola (1988) in the time domain, later, Song et al. (1995) developed a visco-acoustic waveform inversion

in the frequency domain. In their work, they claim that the attenuation phenomenon can be incorparated easier into forward modelling for frequency-domain than in time domain inversions and that both velocity and attenuation gradients can be computed simultaneously without extra cost. Recently, incorporating seismic attenuation in the framework of FWI have play a crucial role in the FWI world (Kamei and Pratt (2013), Operto et al. (2015)).

Several models for considering attenuation have been proposed in the last decades. The model parametrization in terms of attenuation do not affect the shape of the objective function but it will have an impact in the direction of the gradient and the Hessian approximation, influencing on the algorithm convergence.

In the frequency domain, attenuation is considered by the estimation of the quality factor Q, which can be related to the imaginary part of the complex-valued velocity (Hicks and Pratt, 2001). In this work, the Kolsky-Futterman model is considered (Kolsky (1956) and Futterman (1962)). This model defines the relationship between the quality factor and velocity as:

$$\frac{1}{\tilde{v}(\omega)} = \frac{1}{v(\omega)} + \frac{1}{v(\omega)Q\pi} \ln|\frac{\omega_r}{\omega}| + \iota\frac{sgn(\omega)}{2v(\omega)Q}$$

where v and Q represent the phase velocity and the quality factor at the reference frequency w, respectively.

When solving the inverse problem, the velocity term is found in the diagonal of the impedance matrix. Coefficients given by:

$$C_{1i} = \omega^2\rho^{-1}v^{-2}(1 + \frac{1}{Q_i\pi} \ln|\frac{\omega_r}{\omega}| + \iota\frac{sgn(\omega)}{2Q_i})^2$$

However, Song et al. 1995 also claimed that the waveform inversion for attenuation represents a more challenging problem than velocity inversion and that the model gradients

for velocity and attenuation parameters are coupled in frequency-domain waveform inversion. This lack of independent parameter resolution is considered by Operto et al. (2013) as "trade-off".

An alternative approach to improve this "trade-off" is to invert for attenuation, only after retrieving a sufficiently accurate velocity model. An approach termed as "sequential" inversion by Kamei and Pratt (2013). The initial velocity estimation is performed by fixing an starting attenuation model and it seems to have success in Pratt et al. (2004)

In our work we have considered attenuation by a monoparameter attenuation factor (Q) inversion and a multiparameter (P-wave velocity and attenuation factor Q) inversion and explore both the "simultaneous" and "sequential" approaches to minimize the "trade-off" and produce better velocity and attenuation models.

3.5 Time-lapse FWI

We have applied both a "parallel" and "cascade" approach to analyze the time-lapse changes between the vintages for both Inline 1859 and Inline 1874.

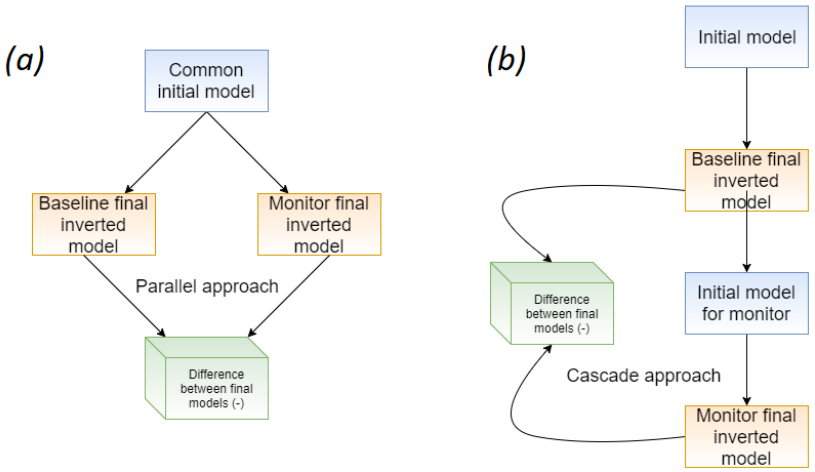

Figure 3.4: Sketches of the parallel approach (a) and the cascade approach (b) applied in FWI.

Figure 3.4, exemplifies the approaches considered in our work.

Chapter 4

Implementation and results of the FWI method

4.1 FWI on the synthetic case

In a first stage, the competence of the algorithm is measured by using a realistic synthetic case of the Sleipner field (Romdhane et al., 2014) . An acquisition geometry with a maximum offset of approximately 3.2 km is emulated, with 160 receivers recording every shot along the profile with a separation of 20 meter between them. The source spacing is of 40 meters for total of 80 sources modeled. The source used for the forward modeling is estimated as a Ricker wavelet.

A total of fifteen (15) frequency components were inverted between 10 and 45 Hz with a maximum of 10 iterations per frequency.

4.1.1 The reference model

Since we use a local optimization scheme, the starting model has to be in the vicinity of the most likely model (Tarantola, 1984). Therefore, as a starting model for inversion of the

pre-injection data from 1994 we use a "smoothed version" of the true synthetic one. (Figure 4.1.a) . This initial model is shown in Figure 4.1.b. The quality factor and the density were set as constant values.

Figure 4.1.c shows the velocity model for the final iteration at 45Hz. The method clearly converged to a possible solution, with an obvious increment in detail of the updated model. The FWI algorithm has the capability to resolve thin layers of around 25 meters-thick with an increment in the maximum P-wave velocity estimate.

Several tests were performed with varying the parameters for: smoothing, S/N of the source and griding of the model, in order to verify how robust is the algorithm in handling variations of these parameters.

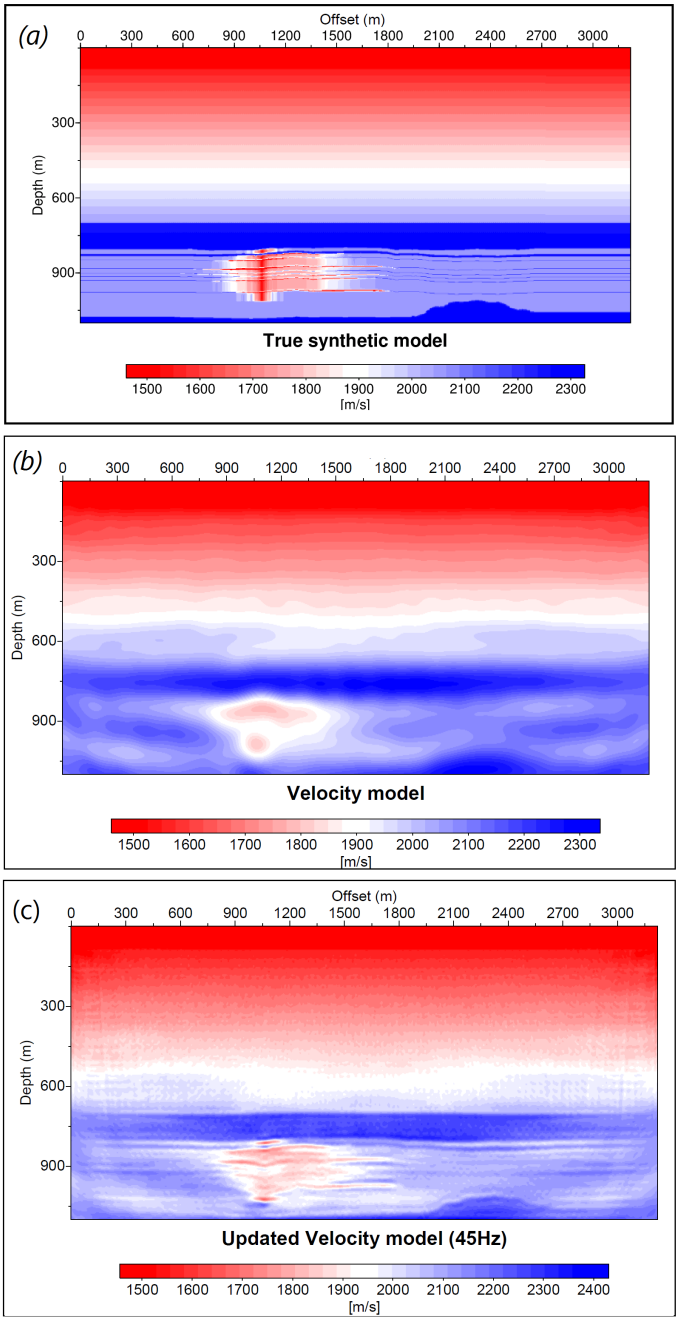

Figure 4.1: (a) "True" synthetic model. (b) Initial reference velocity model c) Final updated model at 45Hz

4.1.2 Smoothing parameters

A smoothing in a damped least squared sense is applied to the initial velocity model of the synthetic case. The aim of this smoothing is to analyze how big the variations of the starting point can handle the FWI algorithm. Two smoothed versions of the initial model were used as the new starting points for two different inversions. Figure 4.2 summarizes the initial models and the final updated velocity models after the method is applied.

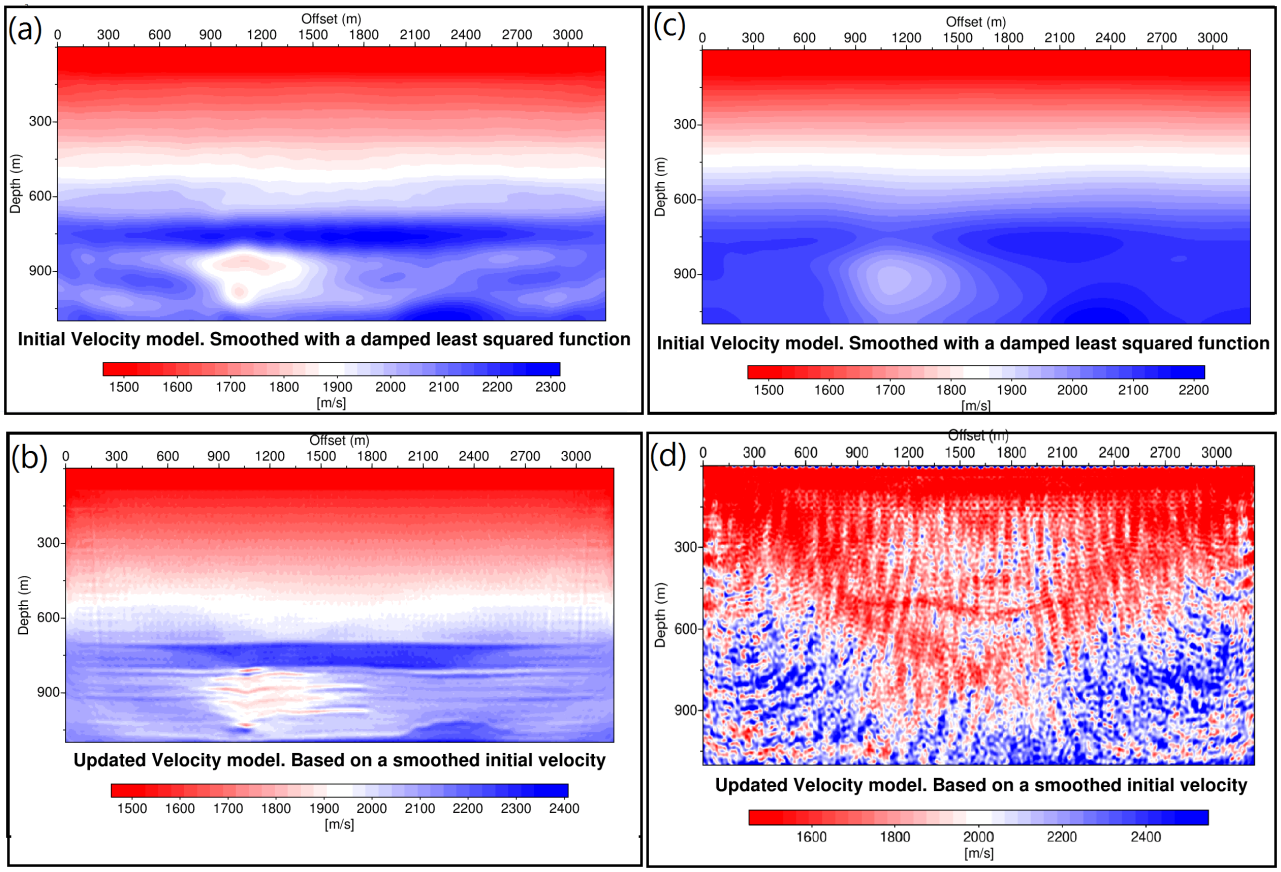

Figure 4.2: a) Initial velocity model for the first case, with a damping parameter of r=10 and the obtained updated velocity model at 45 Hz (b). c) Initial velocity model for the second case, with a damping parameter of r=30 and the obtained updated velocity at 45 Hz (d).

Based on the first version of the initial model (Figure 4.2.a), the method handled well the variations on the initial model imposed by the smoothing process, clearly converging to a solution which is not so far from the reference model shown in Figure4.1. On the other

hand, Figure 4.2.c shows an initial model smoothed with a of r=30 in both directions. The FWI algorithm might have converged to a local minima, yielding a velocity model very far from the one shown in Figure4.1, with no clear spatial distribution of the P-wave velocities (Figure4.2).

As mentioned above, the inversion is solved using a local search method, these kinds of methods rely on a starting point (initial model) that is in the vicinity of the global minimum. The smoothing can be seen as a filter applied to the initial model, implying a less reliable initial point. The starting point considered in Figure 4.2.c, might be too far from the global minimum of the problem.

4.1.3 S/N ratio of the source

According to Virieux and Operto (2009), the exact source excitation is generally unknown and must be considered as an unknown of the problem. In order to verify how robust is the code with handling noisy sources, two tests with different signal to noise ratio were implemented. Figure 4.3 summarizes the two cases analyzed.

As seen in Figure 4.3, the FWI algorithm is robust enough to handle noise in the signal with a S/N ratio of 50, yielding a model with a well-defined spatial distribution of the P-wave velocities and able to resolve the thin layers emulated as the sand layers within the Utsira Fm and where the CO2 is expected to be accumulated (Figure 4.3.a). However, we can find areas in the final updated model with presence of noise (highlighted in black circles) that were not visible in the reference model (Figure 4.1).

For the second case, with a signal to noise ratio of 50, the noise induced by the source dominates the result of the inversion (Figure 4.3.b). This is a way of measuring how sensitive the algorithm is to handle noisy sources.

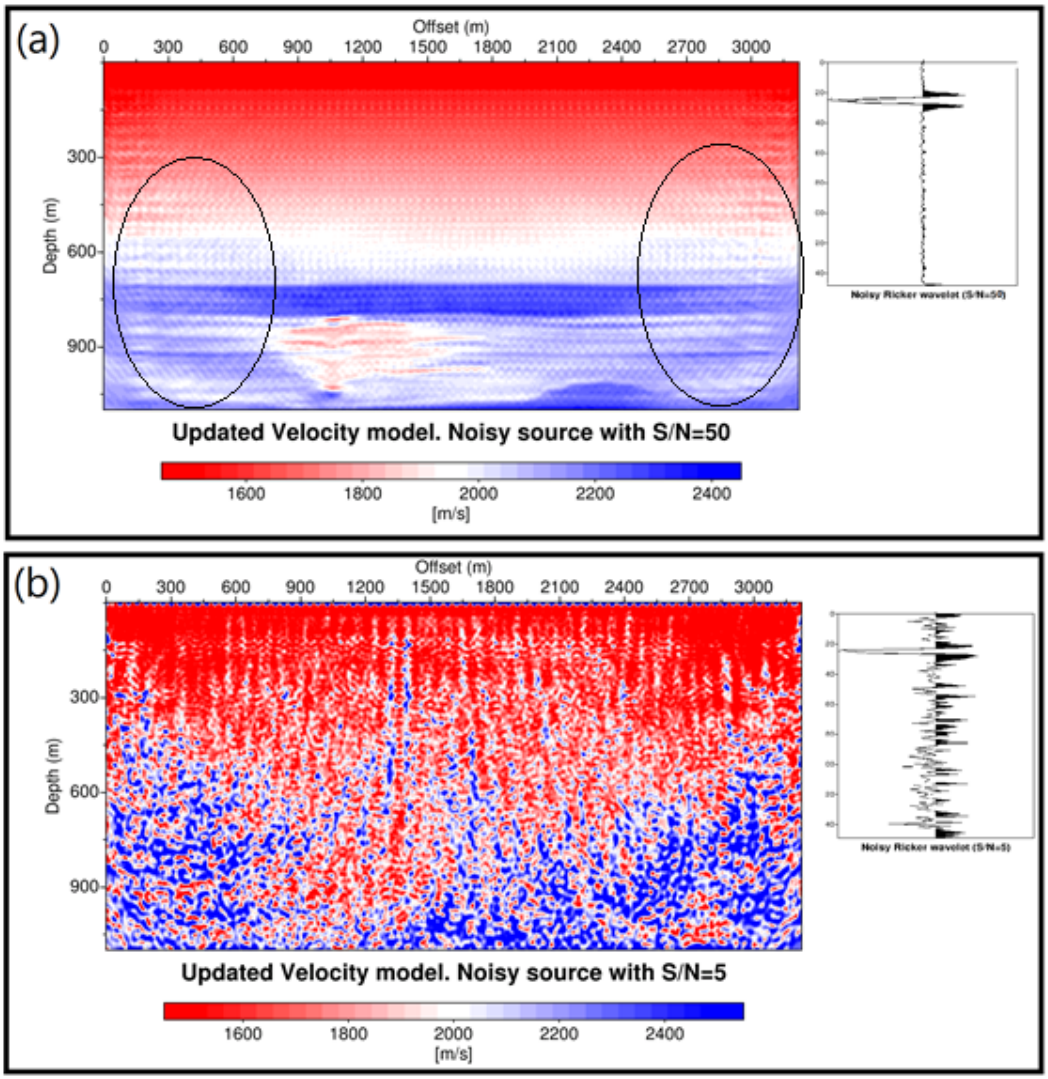

Figure 4.3: Results of the FWI method using a source with S/N ratios of 50 (a) and 5 (b). Both cases are based in a noisy ricker wavelet.

4.1.4 Decimation ratios

The griding used to discretize the space is a 3 by 3 meters in x and y direction. By changing the decimation ratios of the model, we are producing a change in the model gridding. A coarser gridding should result in less discretization points and less computation time. Two cases were studied, with equal decimation ratios in both directions (x and y). A first case using a value of 3 and a second case using a value of 4, this can be translated as using new grids of 6x6 meters and 12x12 meters, respectively. The results are shown in Figure 4.4

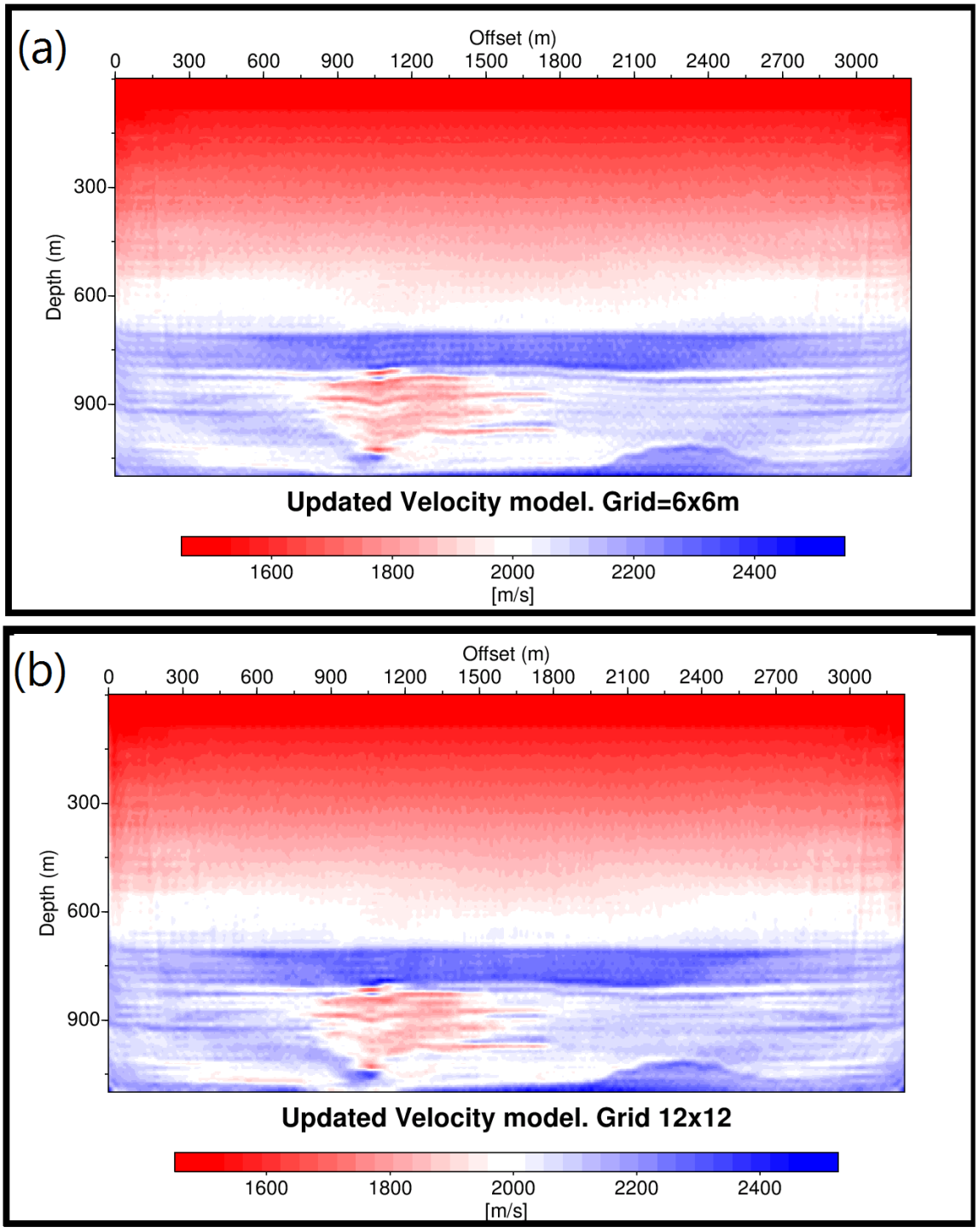

Figure 4.4: Results of the FWI method applied using a different sampling grid of 6x6 meters (a) and 12x12 meters (b)

The FWI algorithm yields very good results using both 6x6 and 12x12 meters squared grid (Figure 4.4). The reason why there are no gain or loss of information by considering a

coarser grid could be linked to the spatial resolution of the method.

The maximum resolution of the FWI method can be related to half of the minimum wavelength considered (Virieux and Operto, 2009) . This minimum wavelength can be found by:

$$\lambda_{min} = \frac{V_{min}}{f_{max}} \tag{4.1}$$

with a maximum resolution given by:

$$\text{Max Resolution} = \frac{\lambda_{min}}{2} \tag{4.2}$$

Where $Vmin$ is the lowest velocity considered in the model, in our case of approximately 1300 meters per second and $fmax$ denotes the highest frequency inverted of 45 Hz. This gives a minimum wavelength of around 28.8 meters implying a resolution of the FWI method of approximately 14.4 meters.

The highest grid considered in our test cases was of 12 meters, being this value below the maximum resolution of the FWI method and hence, not affecting the inversion process.

4.2 2-D FWI on real data from Sleipner field.

The FWI results from the synthetic studies are sufficiently satisfying to justify an application of the method on real-data sets. Once, most of the parameters considered within the FWI method were analyzed and certain values were selected, we proceeded to apply the method using two vintages from the Sleipner data set. Two inlines were extracted from each vintage:

1. "Baseline": Dataset obtained after a seismic survey performed in 1994 (2 years before the injection of CO_2).
    - Inline 1859
    - Inline 1874
2. "Monitor": Dataset acquired in 2008 (12 years after the start of the injection of CO_2).
    - Inline 1859
    - Inline 1874

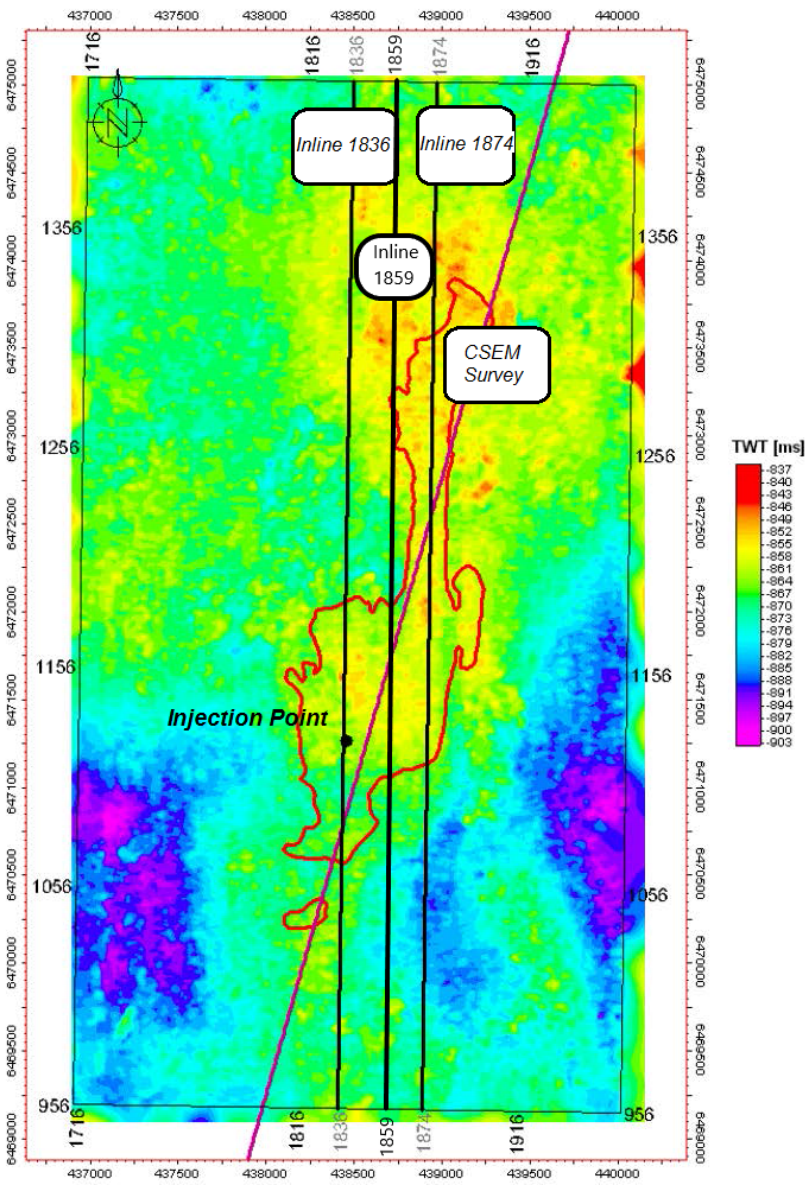

Figure 4.5: Location of the Inlines 1859 and 1874, extracted from the Sleipner data sets.

As shown in Figure 4.5, these inlines were selected in order to compare the expected CO_2 plume distribution.

4.2.1 Pre-processing and initial velocity model

According to Hicks and Pratt (2001), since the FWI method, in theory, considers all forms of waves recorded by the seismogram, one of the advantages is the low data processing required before the application of the method. The pre-processing sequence aims basically

to remove some noise in the data and keep the true amplitudes of the traces.

Pre-processing

The routine is very simple, consisting of basically 4 steps:

1. Removing the T^2 divergence compensation: As a common routine in a the processing of the seismic data, a T^2 gain function is applied to compensate for geometrical spreading and attenuation. Since the FWI relies on the true amplitudes, this effect is removed by applying an inverse function T^{-2} to the data set.

2. Bandpass filter: Since we are inverting for frequencies from 8 Hz up to 30 Hz a bandpass filter is applied with a low frequency cut-off of 6Hz and a high frequency cut-off of 35Hz

3. Top mute: Muting the data before the first arrivals

4. Offset discrimination: A filter of the data to only consider offsets larger than 320m was applied to the data set. This discrimination is mainly due to the lack of illumination at the sides of the acquisition survey

4.2.2 P-wave inversion.

Multi-scale approach and frequency selection

As stated above, a multi-scale approach is applied within the FWI on frequency domain, aiming to prevent the cycle-skipping effect of the data (Virieux and Operto, 2009). Therefore, the FWI consist of successively inversions in which the frequency will be gradually increased. A total of thirteen mono-frequency groups were selected for the FWI, ranging from 8 Hz to up to 35 Hz with 10 iterations per frequency. Following the approach described by Sirgue and Pratt (2004).

Figure 4.6, shows three sequential inversions of the Inline 1859 extracted from the 2008 vintage. Where the frecuency is increased from (a) to (c). The inverted model in (a) is used as initial model to obtain the final inverted model in the next run, being this applied iteratively until the highest frequency considered. The final model (4.6c) is obtained after 130 iterations, with a maximum frequency considered of 35 Hz. It is easy to notice that as long as the frequency content considered increase, the resolution of the model increase, enabling to interpret several layers and a low-velocity zone (LVZ) (black rectangle in Figure 4.6 that might be linked to the injection of CO_2 within the Utsira formation (Romdhane et al., 2014).

In addition, several noisy zones are interpreted as well as oscillations in the sea bottom. This type of noise is attributed to the geometry of the acquisition setup and the nature of the waves, which prevent the recovery of the information on the sides of the models (represented by orange ovals in Figure 4.6).

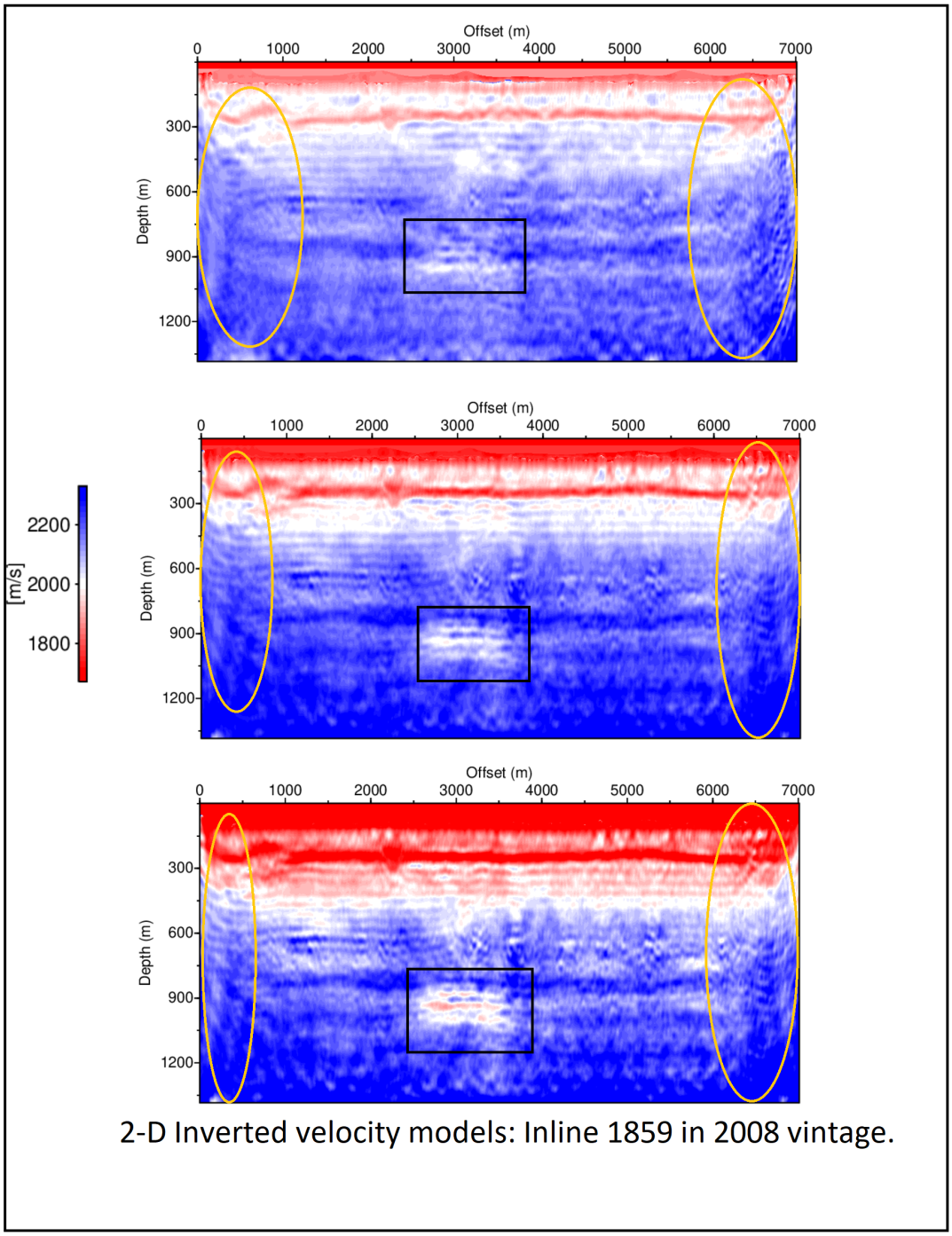

Figure 4.6: Inverted P-wave velocity models with different content of frequency. Gradually increasing from 8 Hz (a) up to 35 Hz (c).

Impact of the initial models

Starting models for real data experiments require a higher degree of accuracy due to the ill-posed nature of the problem (Ravaut et al., 2004). The initial models considered are obtained after the conversion from stacking velocities to interval velocities in depth (Figure 4.7. As mentioned before, the starting model must be in the "neighbourhood" of the global minimum of the objective function, so that the inversion can converge correctly towards the true global minimum.

The initial models have dimensions of 1400 m deep and 7000 m in the horizontal direction. The grid sampling is 12 m on each direction, resulting in approximately 272.183 grid points.

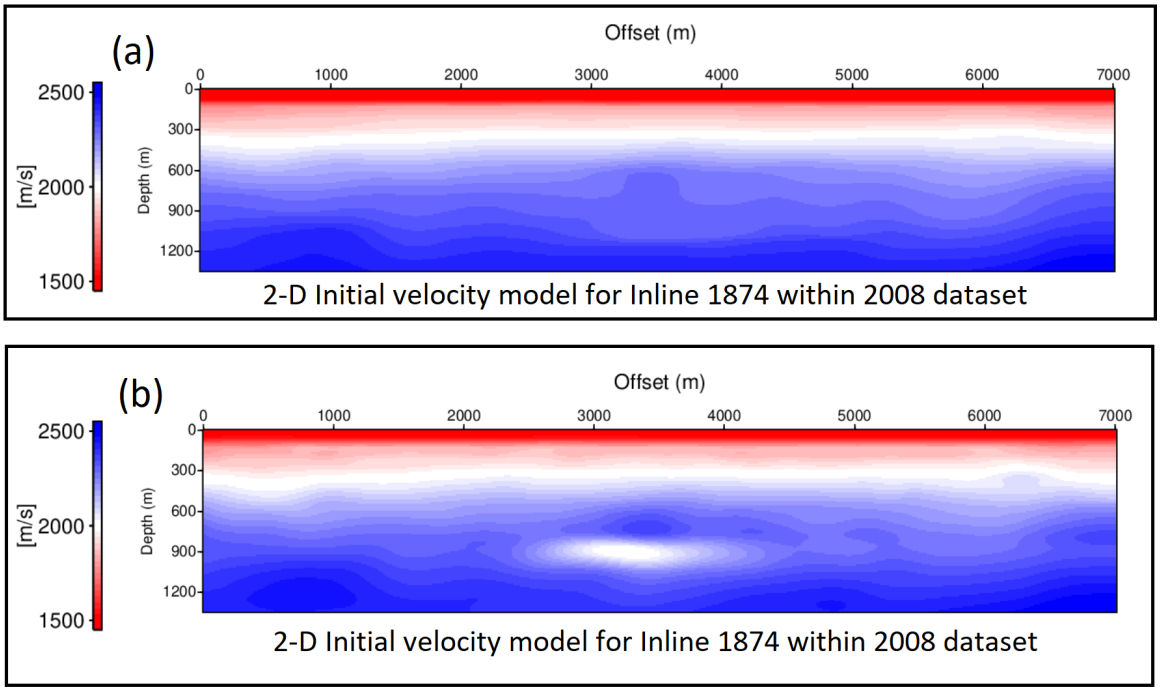

Figure 4.7: Initial velocity models obtained after transforming stacking velocities to interval velocities for both "baseline" (a) and "monitor" (b) datasets.

In order to proof the robustness of the method regarding the initial model, two multi-scale monoparameter (P-wave velocity) inversions were applied to the 1874 Inline from the "monitor" dataset. Where the only difference was the initial model: A first inversion consid-

ers as initial model, the velocity model obtained for the 1994 dataset (Figure 4.7a) after the transformation of the stacking velocities. And a second inversion considers as initial model, the obtained velocity model after transforming stacking velocities for the 2008 dataset (Figure 4.7b). In other words, a FWI is applied to the "monitor" data set using both the velocity model corresponding to the "baseline" and to the "monitor" dataset.

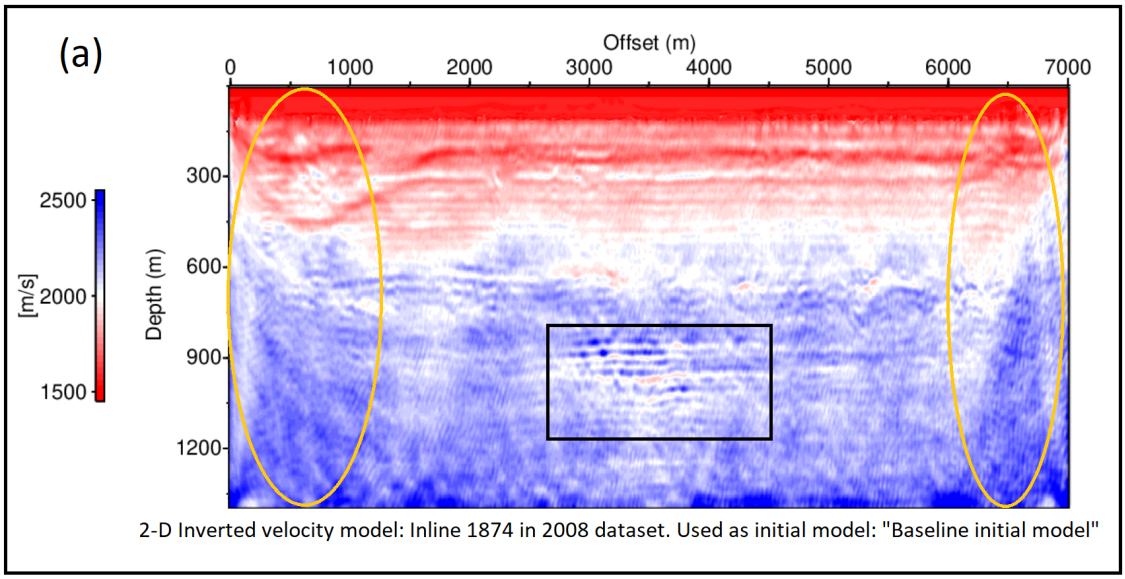

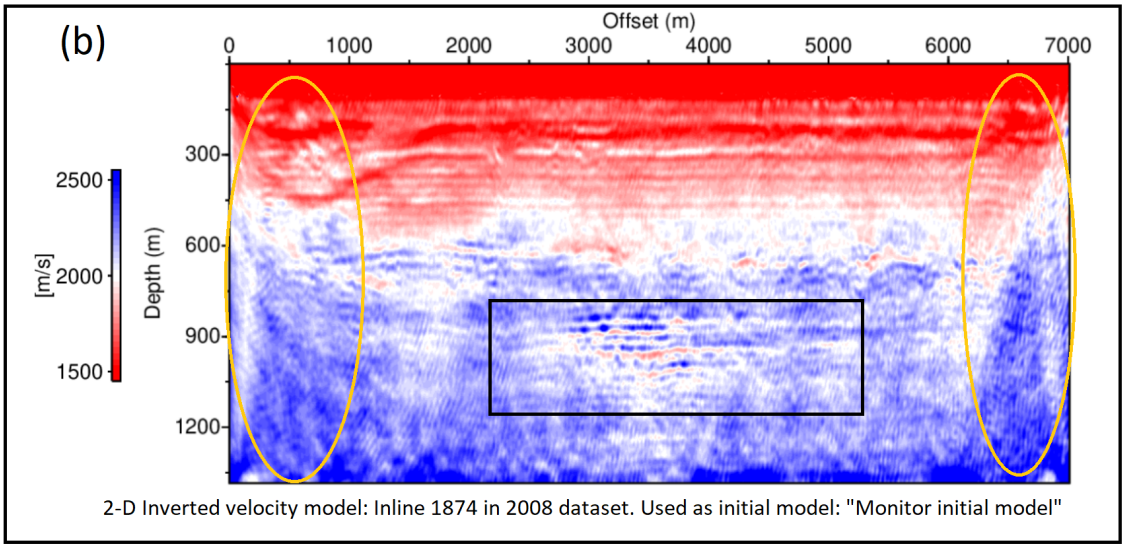

Figure 4.8: Results of the FWI method applied using: (a) Initial velocity model obtained after transformin stacking to interval velocities for the 1994 dataset (b) Initial velocity model obtained after transformin stacking to interval velocities for the 2008 dataset

Figure 4.8 shows the results of the inversions for the Inline 1874 extracted from the 2008 vintage of the Sleipner dataset. The final inverted velocity models were obtained after 130 iterations (10 iterations per frequency).

The method converged to a reasonably accurate solution, showing an improvement in the resolution of the velocity models, compared to the initial models considered (Figure 4.7). Both results consist of several layers (mostly horizontally flat) throughout the model, which can be distinguished by their velocity differences.

The clearest difference in the models obtained, is the low-velocity zone (black rectangle in Figure 4.8) related to the effect of the injected CO_2 (Romdhane et al. (2014)). Based on the velocity model obtained after transforming stacking velocities into interval velocities for the 2008 vintage (Figure 4.7b), the FWI were capable to resolve a better estimated lateral extent of the CO_2 plume and its internal geometry. On the other hand, Figure 4.8a shows the result based on the initial model obtained for the 1994 vintage, where the FWI fails to properly resolve the expected effect of the injected CO_2 gas.

Moreover, the gas bearing layers within the low-velocity zones (LVZ) present a lowest value of P-wave velocity of approximately 1890 m/s for the first case (Figure 4.8a) and 1780 m/s for the second case (Figure 4.8b), being both overestimated in comparison to the value obtained by Carcione et al. (2006) of 1500 m/s.

Updating the density

In the previous results, the density (ρ) was kept constant by using a uniform density model. Compared to P-wave velocity, the density is more difficult to invert by FWI (Butzer, 2015). However, we decided to perform a FWI where the density model is updated after each iteration by using the well-known Gardner's equation (Gardner et al. (1974)):

$$\rho = aV^{\frac{1}{4}} \tag{4.3}$$

where ρ is in g/cm^3 and a is 0.31 when the velocity V is in m/s or 0.23 when V is in ft/s.

All the results obtained after FWI were satisfactory, keeping a very good relationship between the structures and expected values of P-wave velocity throughout the model.

In the models from the Inline 1859 (top of Figure 4.9) of the vintage 1994, the update of the density improved the definition of the layers for the first 600 meters and the model appear to be less noisy (Figure 4.9b) than that without updating the density (Figure 4.9a). Meanwhile, on the 2008 vintage, the LVZ (black rectangle in Figure 4.9 (c) and (d)) is better characterized, with a clear distinction of at least 3 gas bearing layers with a lowest velocity of 1770 m/s.

However, the updating of the density added some artifacts, specially in the first 400 meters of the model (orange rectangle in Figure 4.9d)

When comparing the results obtained after the density update (Figure 4.9f) in the Inline 1874, no signs of improvement were identified from that shown in Figure 4.9e. On the contrary, it adds artifacts in the shallowest part of the model (orange rectangles in Figure 4.9f). The same story can be related to the 2008 vintage results, the LVZ in the model obtained after the density update (Figure 4.9h) lacks of resolution compared to the LVZ found in Figure 4.9g. It also presents less continuity on the shallow part of the model (orange rectangle in Figure 4.9h), compared to the model obtained by keeping a density value fixed (Figure 4.9g).

An important result from these test was the extension of the low-velocity zones. Larger (horizontal direction) velocity anomalies or low-velocity zones are found in the inline 1874 (Figure 4.9g and h), compared to those found in the inline 1859 (Figure 4.9c and d). In

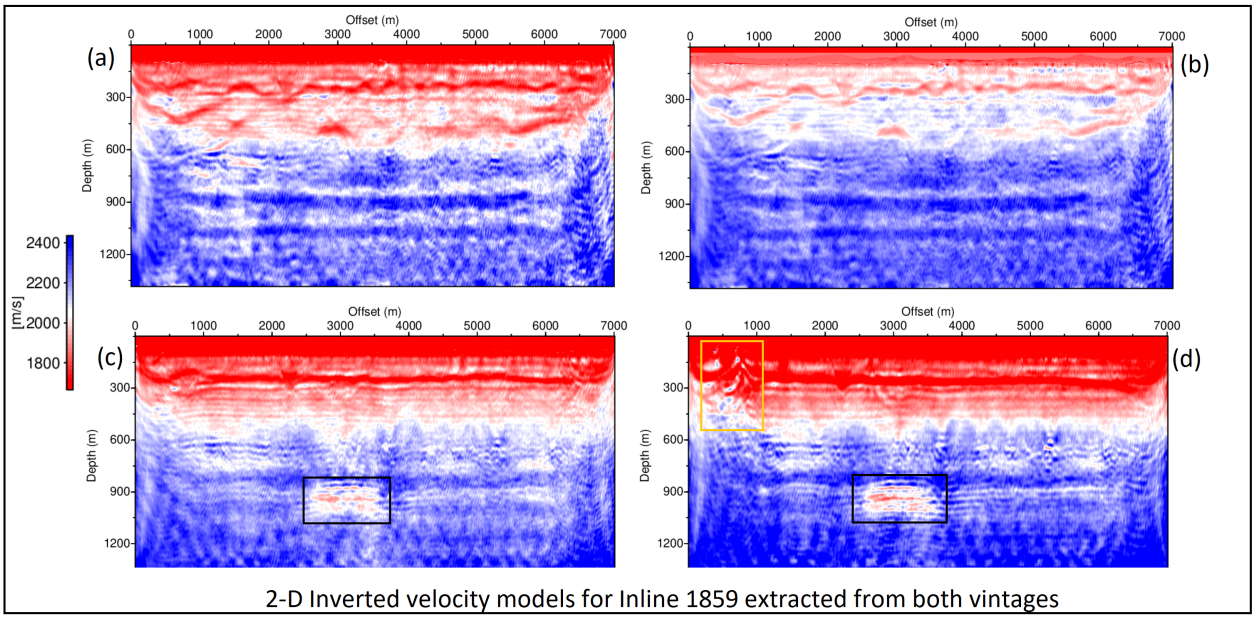

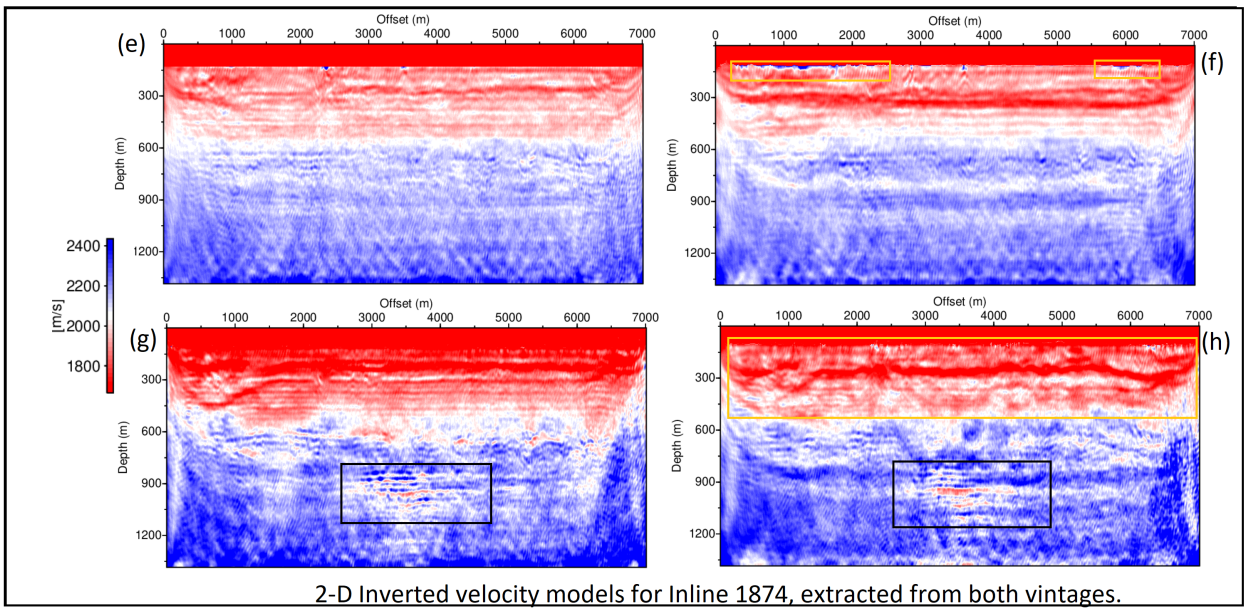

Figure 4.9: Inverted velocity models for Inline 1859 (top) and 1874 (bottom), extracted from both the "baseline" ((a), (b), (e) and (f)) and "monitor" ((c), (d), (g) and (h)) vintage. (b), (d), (f) and (h) were obtained after updating the density model by the Gardner's equation. (a), (c), (e) and (g) were obtained without updating the density model.

agreement to the distribution of the CO_2 plume within the zone (Figure 4.5),

Computationally speaking, it took 1.21 times the time consumed to obtain the final result

of the inversion while updating the density. Furthermore, the objective function decreased with a slower rate compared to the inversion with a fixed value of the density (Figure 4.10).

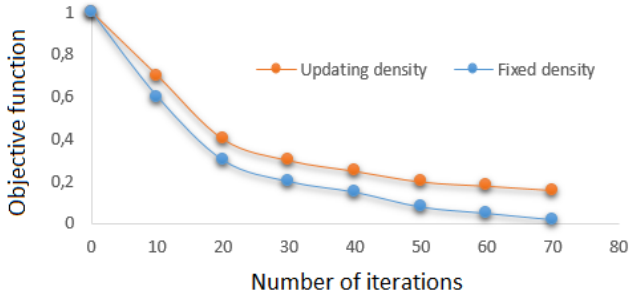

Figure 4.10: Normalized objective function decay for the Inline 1859 extracted from the 1994 vintage.

The fact that updating the density do not give any signficant result and increased the computational demand, the density was fixed for the following inversions.

4.2.3 Time-lapse FWI in 2-D.

The initial model obtained after transforming the stacking velocities into interval velocities for the 1994 vintage (Figure 4.7a), was considered as the common initial model in the parallel approach (Figure 3.4a) for both inlines.

On the other hand, as stated above, the "cascade" approach (Figure 3.4b) considered the same initial velocity model when inverting for the baseline dataset but the result of this inversion is then used as the initial velocity model for the monitor dataset.

Figures 4.11 and 4.12 show the time-lapse difference in P-wave velocity values of the models obtained for Inline 1859 and Inline 1874 respectively.

As it can be seen in Figure 4.11a, the biggest change in velocity for the parallel approach are found in the shallowest part of the model (represented by the yellow rectangle) and at the very bottom of the model. Based on the literature (Chadwick et al. (2006), Furre et al.

(2017)), there are no reasons of why such low velocities might be found at these intervals. Therefore, we consider them as artifacts of the method. However, the approach was capable to distinguish a low-velocity zone (LVZ) between approximately 800ms and 1100ms (black rectangle in Figure 4.11a).

The velocity change within the LVZ range between 200 and 300 m/s, which is in accordance to that found by Romdhane et al. (2014). This velocity model is attributed to the changes in P-wave velocity due to the injection of the CO_2 in the Sleipner field.

Similar structures are also found in the result obtained after the "cascade" method (Figure 4.11b). With the same high values on top and bottom of the model. Nevertheless, the model consist of lower velocity difference in general, where most of the model shows differences closer to zero than the previous case. Again, there is a remarkable LVZ in the center-bottom of the model. The difference, however, is bigger than in the parallel approach (Figure 4.11a).

For the inline 1874 (Figure 4.12), the difference between the approaches are more remarkable. In the parallel approach, there is found a much larger low-velocity zone (Figure 4.12a) which is not expected, based on previous work.

The cascade approach, on the contrary, is capable of determine a more constrained LVZ but as it happened to the Inline 1859, a strong artifact is added to the model in the shallowest part of the model (yellow rectangle in Figure 4.12b).

The artifacts or noise-related energy provided by the parallel approach might be due to assumption of a similar level of convergence in both datasets, mainly due to the fixed number of iterations (120 in our case) are carried out. The ill-posed nature of the seismic inversion problem and the several local minima along the objective function makes almost impossible for this condition to happen. When inverting each dataset individually, the quality of the final result might be affected by data quality and non-repeatability of the surveys in question. In other words, after applying the parallel approach, we might end up in different local minima

and the substraction of the two models that are far from each other may result in inaccurate property changes.

On the other hand, the cascade approach has also a remarkable assumption that might not be always fulfilled. The approach assumes a complete convergence of the baseline. Where no more model updates are needed since the differences between the vintages are exclusively caused by reservoir changes. Due to time and computational constraints, a finite and limited numbers of iterations are performed; leading to a convergence of the baseline that rather than being in a global minimum, is found in a local one. Therefore, the residuals found in the baseline might migrate to the monitor dataset when performing the FWI and deteriorating the true time-lapse difference of the models.

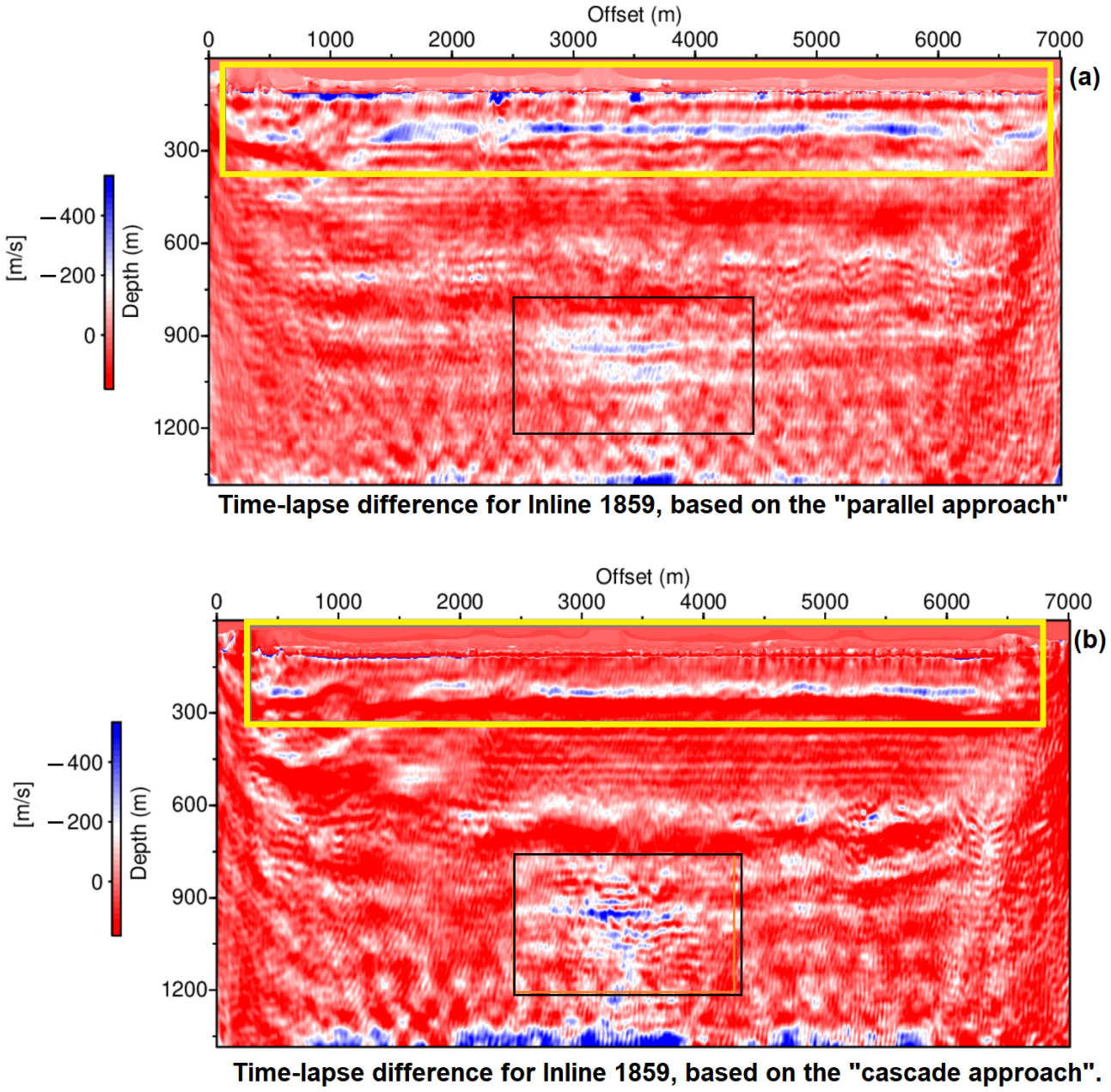

Figure 4.11: Normalized objective function decay for the Inline 1859 extracted from the 1994 vintage.

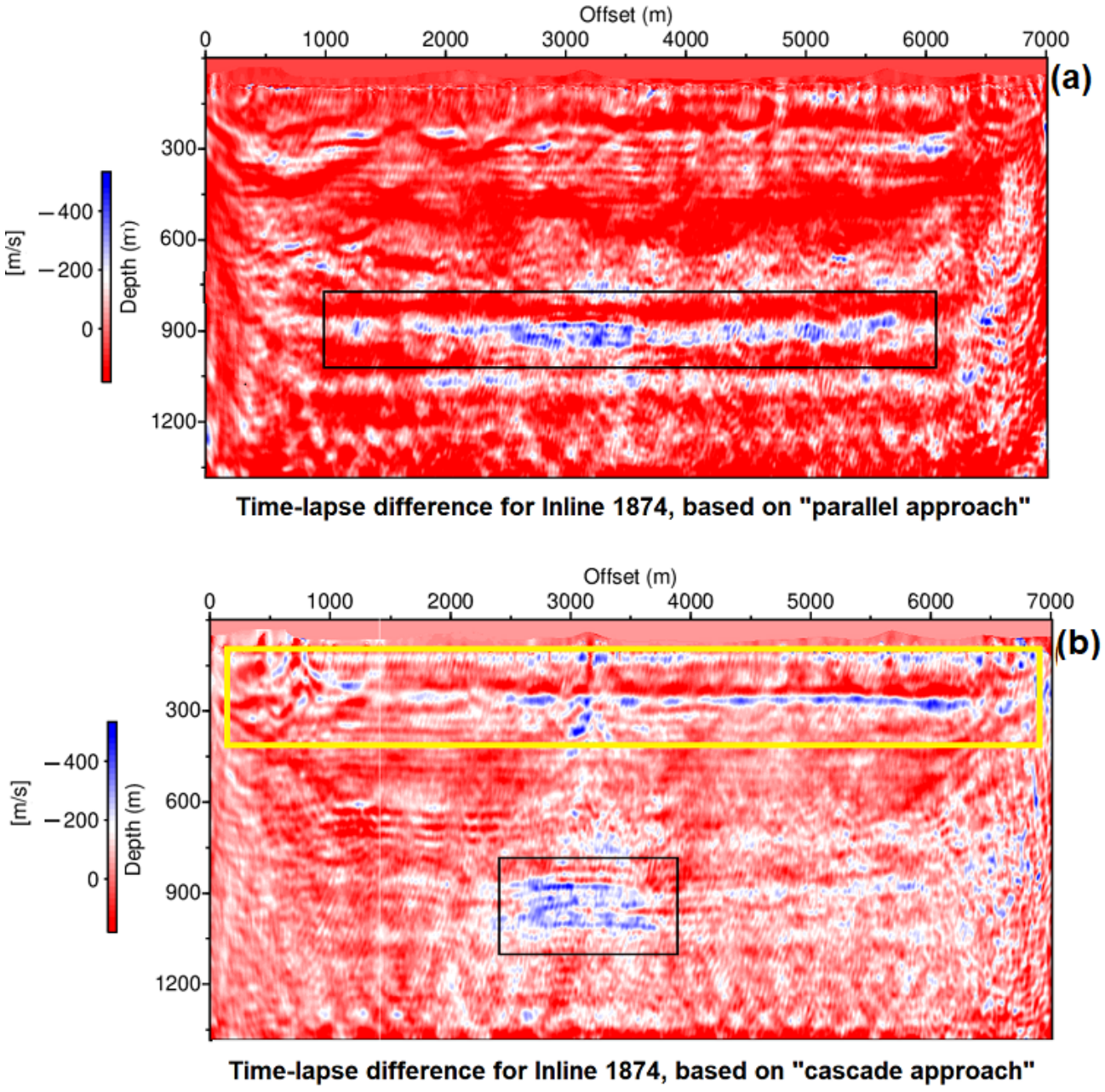

Figure 4.12: Normalized objective function decay for the Inline 1859 extracted from the 1994 vintage.

4.3 2.5-D FWI on real data from Sleipner field.

Several 3D studies have been performed in the last couple of years but the vast majority of the FWI applications are still restricted to 2D approximations, being the dramatic increase in computational costs the main barrier for the use of 3D FWI in real cases.

However, the 2D approximation is unable to explain the scattering phenomenon related to 3D heterogeneous subsurface structures. 3D scattering arising from 3D heterogeneous subsurface structures (Butzer, 2015).

In this work, we have considered a 2.5D Full-waveform inversion, in which the solution of the full 3D visco-acoustic waveform is solved but only 5 planes in the Y space direction are considered. In consequence, the following models have dimensions of 1400 m deep and 7000 m and 5 in the horizontal directions.

In order to save computational time, the grid sampling of the model have been changed to 12m on each direction, resulting in approximately 335.000 grid points.

In addition, fewer frequencies were considered. Maintaining, however, a fully covered wavenumber spectra as it is stated in Sirgue and Pratt (2004). A total of 7 frequencies were inverted, covering a range from 8 Hz up to 20 Hz.

Figures 4.13 and 4.15, show the results of the P-wave velocity inversion, after considering the 3D visco-acoustic wave equation. For all the results, the density and attenuation factor were kept constant.

The results are satisfactory and converge to a clear solution. As expected, the models have much lower resolution that those from the 2-D inversion tests, attributed to the fewer number of frequencies considered by the inversion. Even though the wavenumber spectra is fully covered by the frequencies selected, the redundancy of the data plays an important role

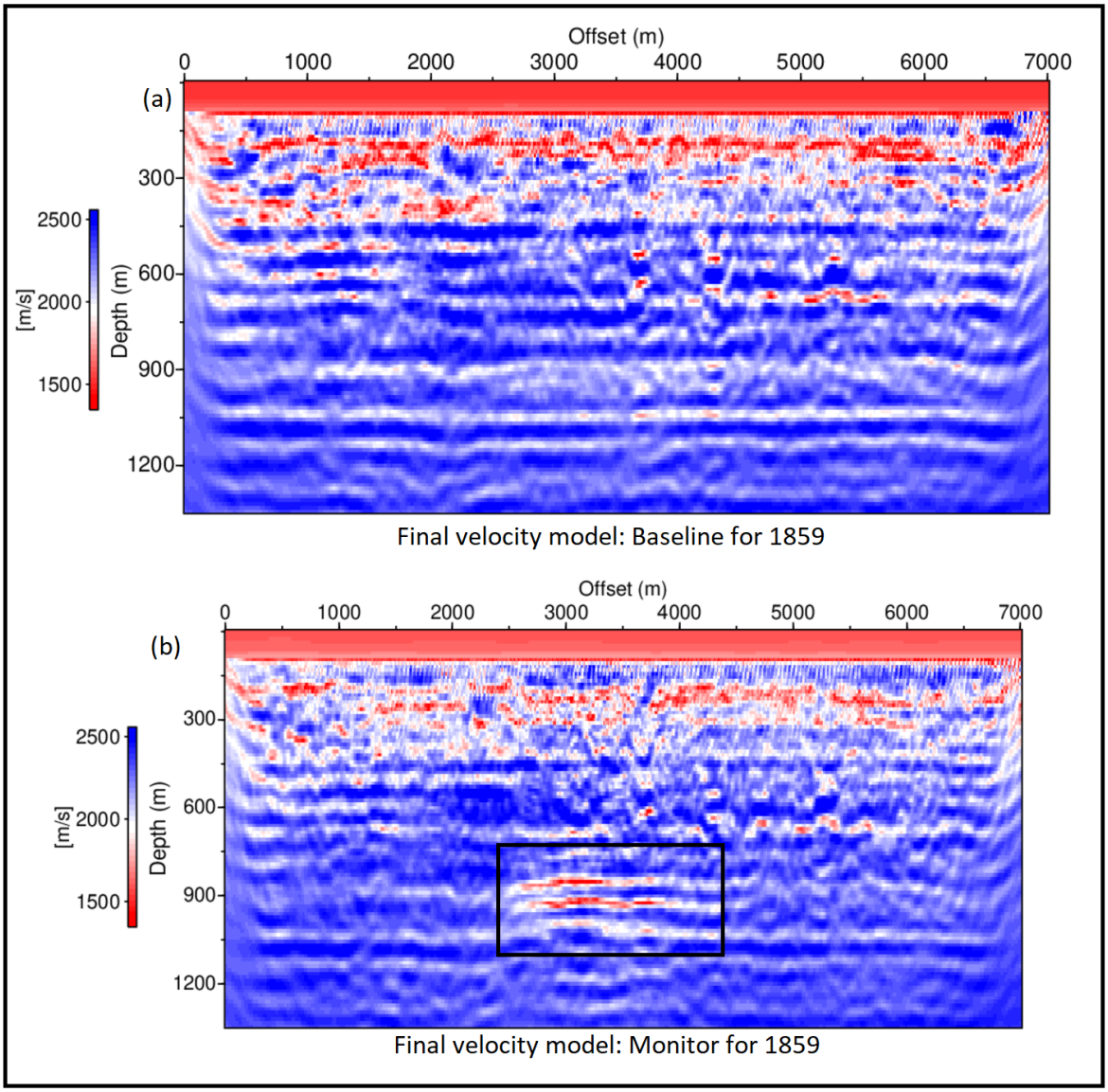

Figure 4.13: Vertical slice at the middle of the 2.5-D model, for Inline 1859 extracted from the 1994 vintage (a) and 2008 vintage (b).

in the quality of the inversion results. However, the method was capable again to characterize a low-velocity zone for both inline in the 2008 vintage (Figure 4.13b and 4.15b).

One difference from those models in 2-D is that the LVZs have a even lower P-wave velocity (1720 m/s), considered a better estimation of the parameter, compared to the value of 1770 and 1780 from the 2-D tests.

Again, the extension of the low-velocity zones differ between vintages, in accordance to

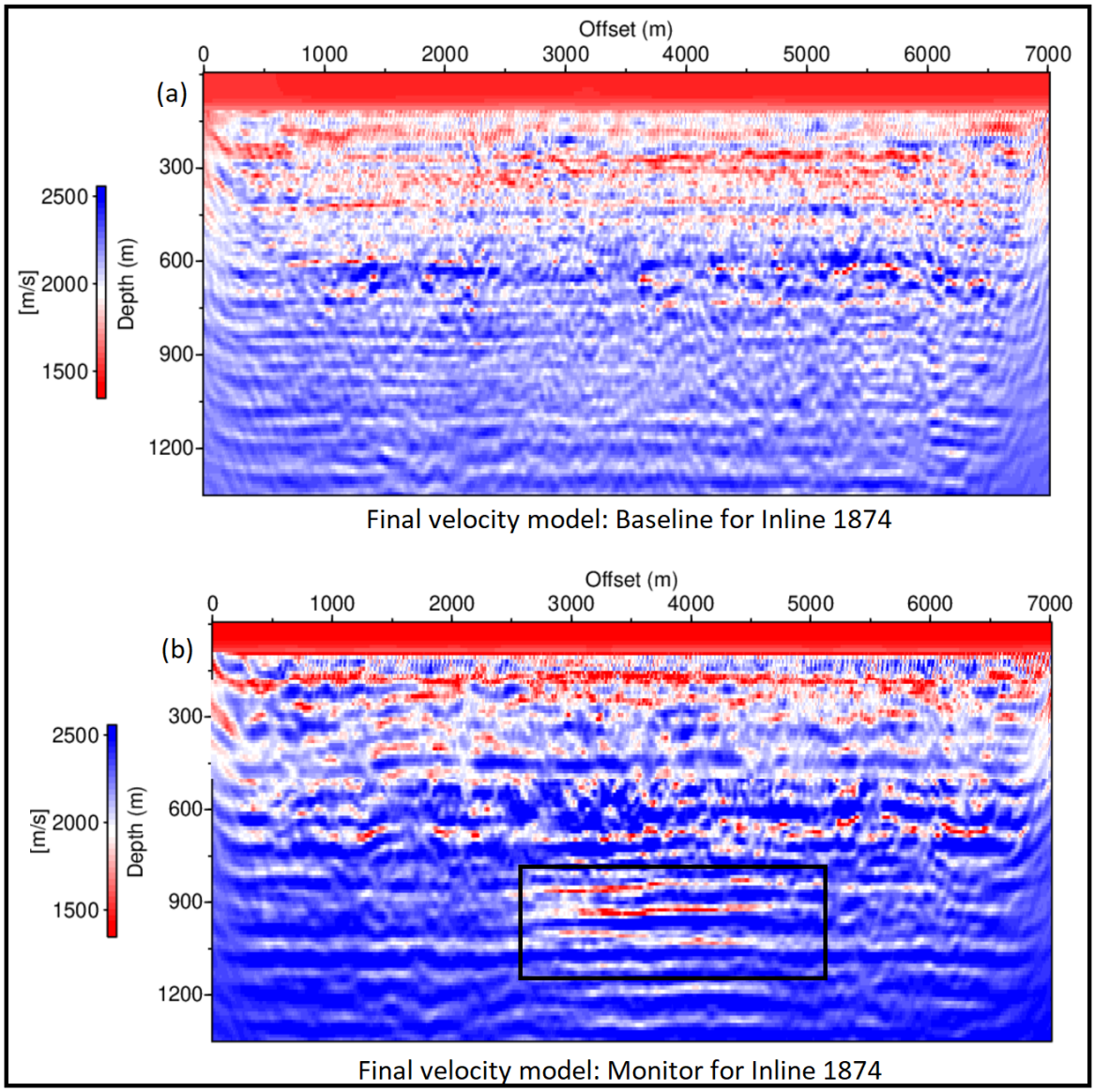

Figure 4.14: Vertical slice at the middle of the 2.5-D model, for Inline 1874 extracted from the 1994 vintage (a) and 2008 vintage (b).

what is expected due to the distribution of the CO_2 plume throughout time (Figure 4.5).

4.3.1 Time-lapse FWI in 2.5-D

Following the results from the time-lapse analysis performed in 2-D, a "cascade approach" was considered over the "parallel approach" for a 2.5-D time-lapse FWI.

Due to time constraints, the study was performed only for Inline 1874. The selection

of this inline was based on a better characterization of the velocity anomaly (Figure 4.15b), compared to that of the Inline 1859 (Figure 4.13b)

Suprisingly, the time-lapse difference for the 2.5D FWI yielded a better result, compared to the 2-D time-lapse analysis (4.12). Although, less frequencies and bigger grid sampling is considered, in addition to the lack of redundancy due to the reduction in iterations compared to the 2-D analysis, the result bears less noise or artifacts induced by the assumptions of the "cascade approach"

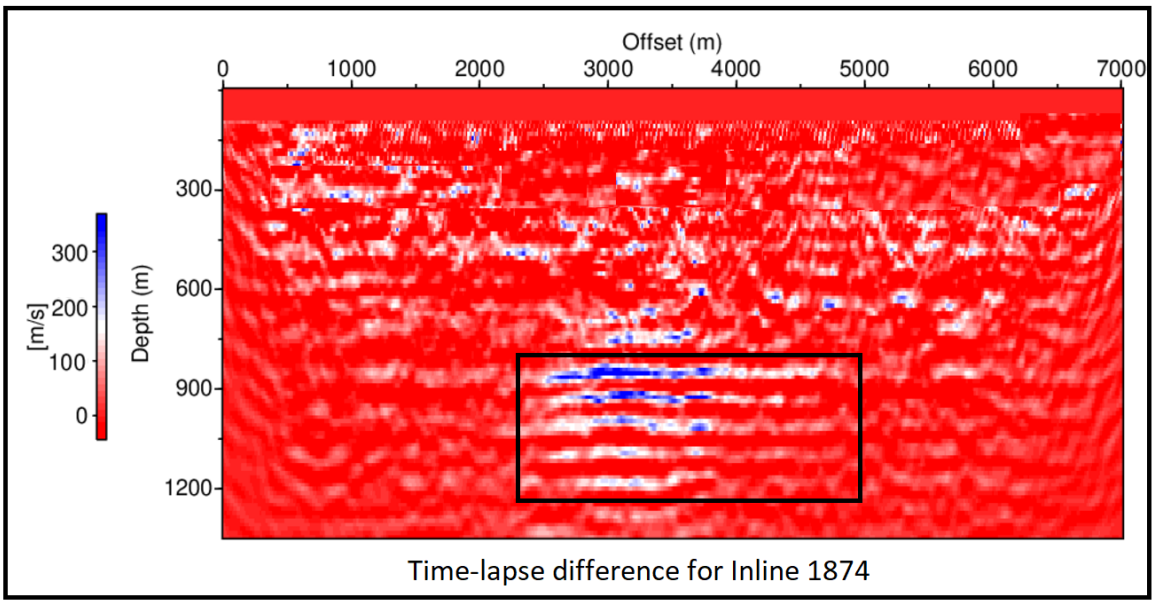

Figure 4.15: Vertical time-lapse difference slice at the middle of the 2.5-D model, for Inline 1874.

4.3.2 Quality factor (Q) inversion

Our last set of inversion runs were related to the study of the attenuation. As stated before, one of the advantages of the FWI in frequency domain is the easy implementation of attenuation in the forward modelling by being related to the complex velocity.

The results from the inversion of Q factor show a quite smooth relationship and horizontally flat distribution of the Q factor. With an increment in the values as the depth increases.

The results from the monitor datasets show a decrease in the quality factor that might be

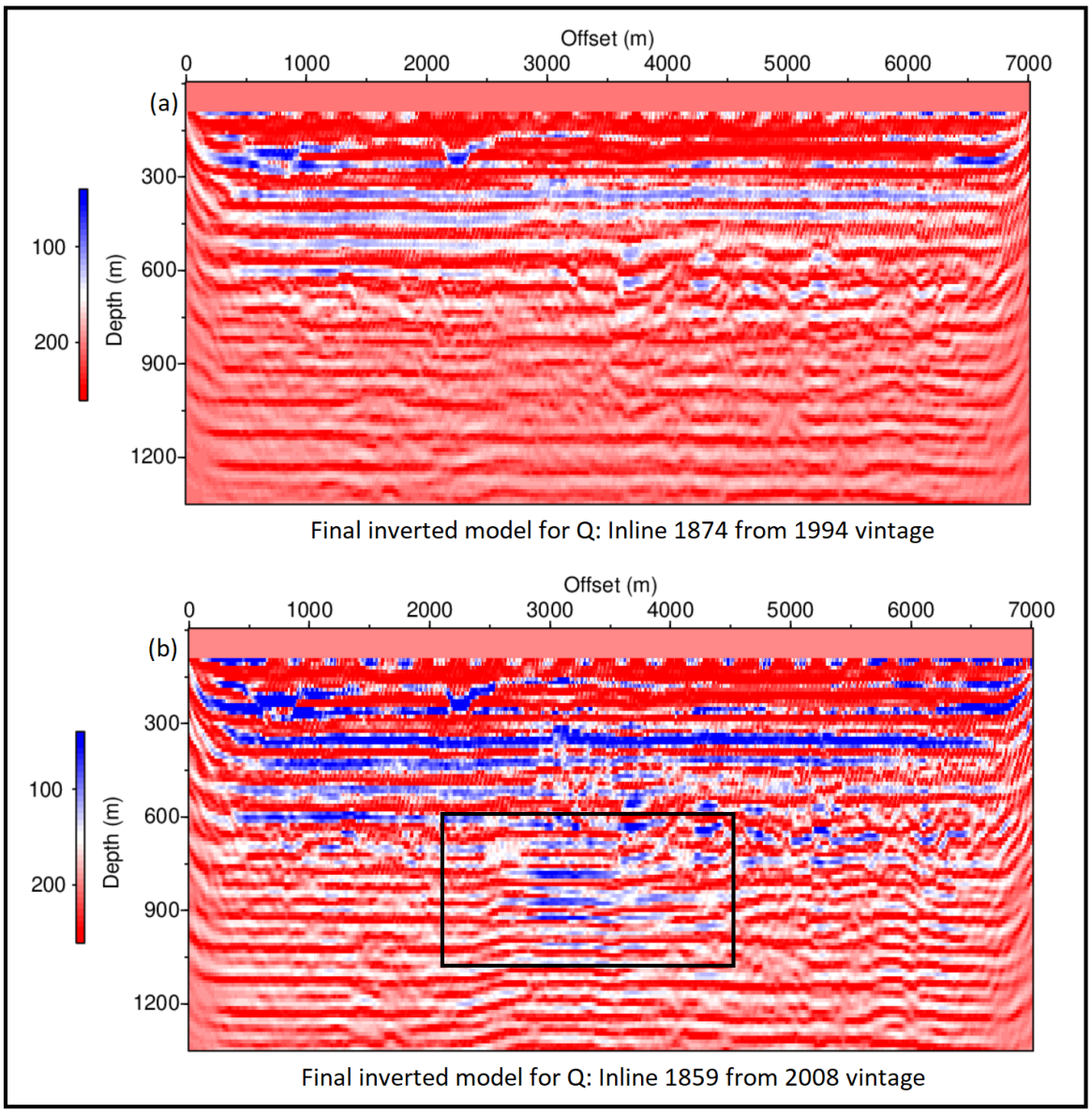

Figure 4.16: Vertical slices of Q factor at the middle of the 2.5-D model, for Inline 1859 in both vintages.

linked to the presence of gas in the zone.

In order to verify the reliability of the results from the quality factor inversion, we decided to performe a multiparameter FWI, considering both P-wave velocity and attenuation factor (Q). Shown in Figure 4.18

As it can be seen in Figure 4.18, there is a huge "trade-off" between the parameters considered by the multiparameter FWI. Being the velocity, the dominant parameter between

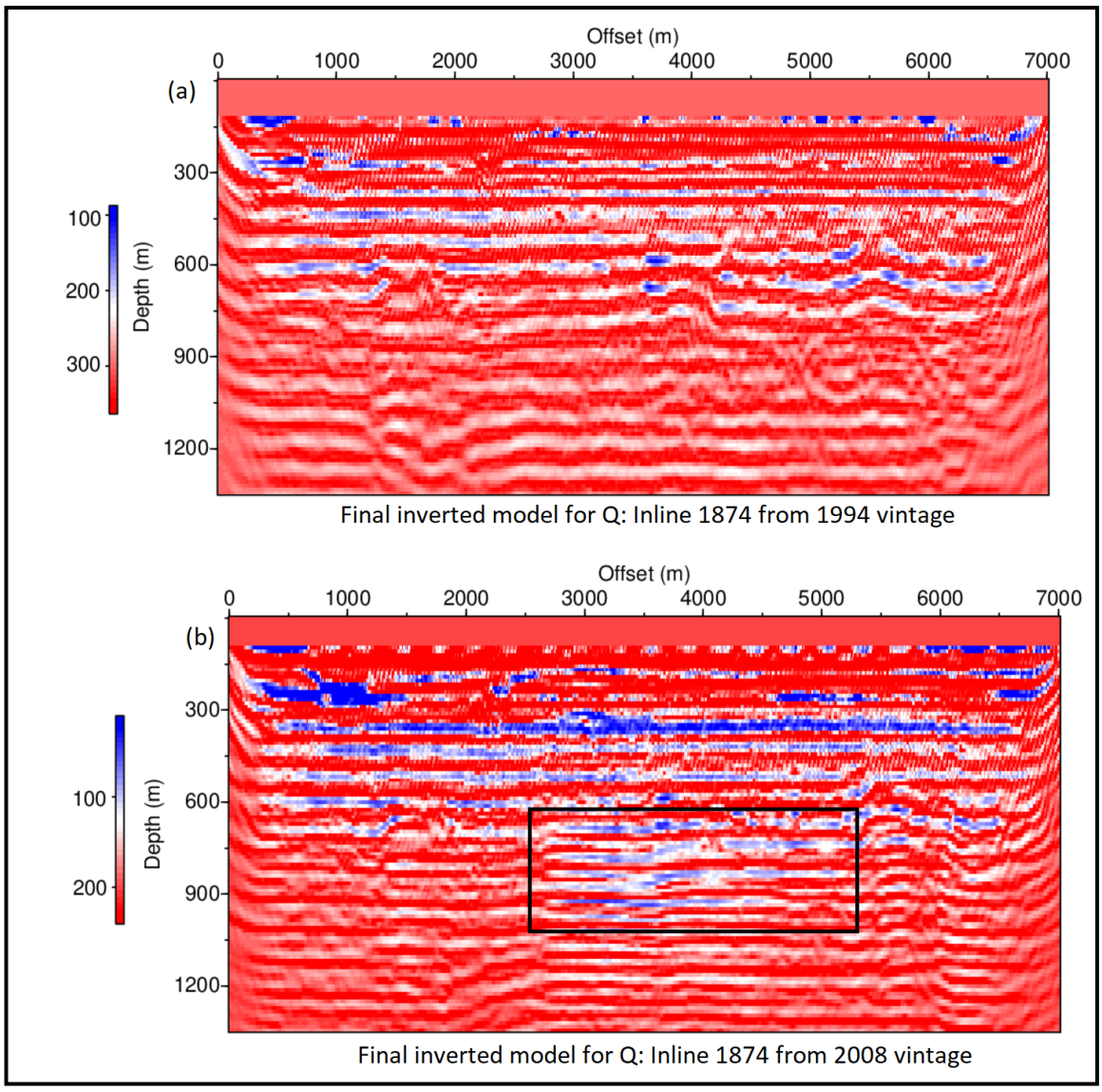

Figure 4.17: Vertical slices of Q factor at the middle of the 2.5-D model, for Inline 1874 in both vintages.

them. Several anomalies have been identified (black rectangles in Figure 4.18) in the P-wave velocity model, which are explicitly shown in the quality factor (Q) inversion.

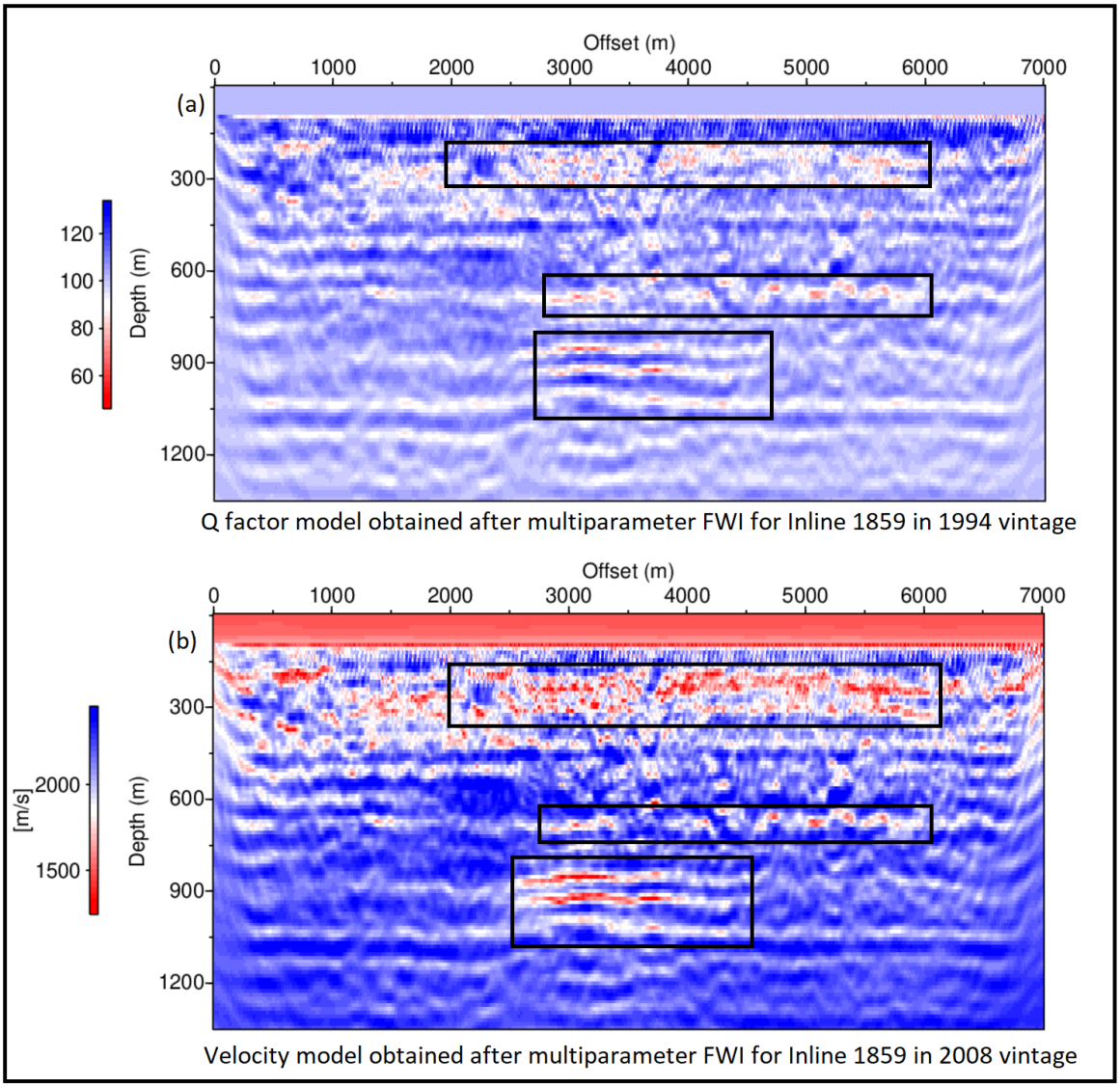

Figure 4.18: Vertical slices of Q factor (a) and P-wave velocity (b) at the middle of the 2.5-D model, for Inline 1859 in 2008 vintage.

Chapter 5

Conclusions

A multi-scale monoparameter and multiparameter Full-Waveform Inversion in frequency domain has been applied considering both 2-D and 3-D visco-acoustic wave equation, for deriving P-wave velocity (Vp) and attenuation factor (Q) models in two inlines extracted from two vintages of the Sleipner Field (1994 and 2008).

The algorithm uses the waveform information from the pre-stack datasets of the Sleipner field recorded in 1994 and 2008 (before and after the injection of had CO_2 started). A pre-processing workflow, aiming to enhance the signal to noise ratio (S/N) without harming the amplitudes, is applied to the data before the application of the FWI method.

In a first stage, several tests were performed on synthetic data, aiming to measure the sensitivity of the algorithm when it comes to handle noisy sources, a less reliable initial model and different spacing grids. From these test, it was found that the algorithm is quite sensitive to handle noise in the sources, having converged to a local minimum when a S/N ratio below 5 is used. It was also found that a starting initial velocity model is critical to avoid cycle skipping and thus convergence to a local minimum. On the other hand, a bigger spacing grid can be used without losing critical information.

The impact of the initial model is also measured in the real dataset by performing a 2-D FWI. Where an improvement in the resolution of the P-wave velocity models were achieved by using as initial model, the velocity model obtained after transforming stacking velocities to interval velocities of the 2008 vintage.

A following test regarding the update of the density were performed, in which no sign of improvement was achieved by using the Gardner's equation to update the density, respect to the velocity. On the contrary, it added artifacts and increased the computational time of the inversion.

Two approaches were applied in order to asses the time-lapse difference of the vintages. A "cascade" approach is considered to give better indication of the lateral extension and change in velocity values due to the injection of CO_2 in the reservoir. However, the results obtained for both approaches bear zones with strong difference in velocity which is not expected to happen. This might be due to the limitation in iterations, different possible local minima for each data set in the "parallel approach" and the assumption that the baseline is fully inverted and its global minimum is achieved before it is used as initial model in the "cascade approach"

Attenuation has been considered by the relationship between the quality factor (Q) and the complex value of the velocity. Results from the attenuation inversion show a smooth behavior of the distribution of the parameter and a decrease in the zone where the gas is expected to be accumulated.

A last inversion consisted in a multiparameter FWI, inverting for both P-wave velocity and quality factor, where a strong "trade-off" between the parameters is shown in the results.

In all the results there is a difference in extension between the low-velocity zone related to the CO_2 plume between the Inline 1859 and 1874.

Bibliography

R. Arts and O. Eiken. Monitoring of CO 2 injected at Sleipner using time-lapse seismic data. *Energy, 29(9), 1383-1392*, 2004.

S. Bachu. Screening and ranking of sedimentary basins for sequestration of CO2 in geological media in response to climate change. *Environmental Geology, vol. 44, pp. 277-289*, 2003.

R. Brossier, S. Operto, and J. Virieux. Seismic imaging of complex onshore structures by 2D elastic frequency-domain full-waveform inversion. *Geophysics, 74(6), WCC105-WCC118.*, 2009.

C. Bunks, F. Saleck, S. Zaleski, and Chavent. Multiscale seismic waveform inversion. *Geophysics, 60(5), 1457–1473.*, 1995.

S. Butzer. 3D elastic time-frequency full-waveform inversion. 2015.

J. M. Carcione, S. Picotti, D. Gei, and G. Rossi. Physics and seismic modeling for monitoring CO2 storage: Pure and Applied Geophysics. *Geophysics, 163, 175–207.*, 2006.

A. Chadwick, R. Arts, O. Eiken, P. Williamson, and G. Williams. Geophysical monitoring of the CO2 plume at Sleipner, North Sea. In Advances in the geological storage of carbon dioxide. *Springer, Dordrecht.*, 2006.

R. Chadwick, S. Holloway, M. Brook, and Kirby. The case for underground CO2 sequestration in northern Europe. *Geological Storage for CO2 emissions reduction.Special Publication of the Geological Society, London, 233, 17 - 28.*, 2004.

A.-K. Furre, A. Kiær, and O. Eiken. CO2-induced seismic time shifts at Sleipner. *Interpretation , vol. 3, no. 3,pp. SS23-SS35.*, 2015.

A. K. Furre, O. Eiken, H. Alnes, J. N. Vevatne, and A. Kiær. 20 years of monitoring CO2-injection at Sleipner. *Energy Procedia, 114, 3916-3926. ISO 690.*, 2017.

W. I. Futterman. Dispersive body waves. *Journal of Geophysical research, 67(13), 5279-5291.*, 1962.

G. Gardner, L. Gardner, and A. Gregory. Formation velocity and density – the diagnostic basics for stratigraphic traps. *Geophysics, 39, 770-780.*, 1974.

H. Hansen, O. Eiken, and T. O. Aasum. Tracing the path of carbon dioxide from a gas-condensate reservoir, through an amine plant and back into a subsurface acquifer. Case study: The Sleipner area, Norwegian North Sea. *in SPE Offhsore Europe, Aberdeen, UK,*, 2005.

J. Helgesen and M. Landrø. Estimation of elastic parameters from AV0 effects in Tau-P domain. *Geophysical Prospecting, 41(3), 341-366.*, 1993.

G. J. Hicks and R. G. Pratt. Reflection waveform inversion using local descent methods: Estimating attenuation and velocity over a gas-sand deposit. *Geophysics, 66(2), 598-612.9.*, 2001.

T. Holloway, H. Levy, and P. Kasibhatla. Global distribution of carbon monoxide. *Journal of Geophysical Research: Atmospheres, 105(D10), 12123-12147.*, 2000.

R. Kamei and R. Pratt. Inversion strategies for visco-acoustic wave-form inversion. *Geophysics. J. Int., 194, 859–894*, 2013.

H. Kolsky. The propagation of stress pulses in viscoelastic solids. *Philosophical magazine, 1(8), 693-710.*, 1956.

P. Lailly. The seismic inverse problem as a sequence of before-stack migrations. *Conference on inverse scattering: Theory and applications: Society for Industrial and Applied Mathematics, 206–220.*, 1983.

M. Little and G. Jackson. Potential impacts of leakage from deep CO2 geosequestration on overlying freshwater aquifers. *Environmental science & technology, 44(23), 9225-9232.*, 2010.

Metivier., R. Brossier, S. Operto, and Virieux. Full waveform inversion and the truncated newton method. *SIAM Review, 59(1), 153-195.*, 2017.

P. Mora. Nonlinear two-dimensional elastic inversion of multioffset seismic data. *Geophysics, 52(9), 1211-1228.*, 1987.

J. M. Nordbotten, M. Celia, and S. Bachu. Injection and storage of CO 2 in deep saline aquifers: analytical solution for CO 2 plume evolution during injection. *Transport in Porous media, 58(3), 339-360. ISO 690*, 2005.

S. Operto, Y. Gholami, V. Prieux, A. Ribodetti, R. Brossier, L. Metivier, and . Virieux. A guided tour of multiparameter full-waveform inversion with multicomponent data: From theory to practice. *The Leading Edge, 32(9), 1040-1054.*, 2013.

S. Operto, A. Miniussi, R. Brossier, L. Combe, L. M´etivier, V. Monteiller, A. Ribodetti, and J. Virieux. Ef[U+FB01]cient 3-D frequency-domain mono-parameter full-waveform inversion of ocean-bottom cable data:application to Valhall in the visco-acoustic vertical transverse isotropicapproximation. *Geophysics. J. Int., 202(2), 1362–1391*, 2015.

. W. M. H. Pratt, R. G. Inverse theory applied to multi-source cross-hole tomography. Part 1: Acoustic wave-equation method. *Geophysical prospecting, 38(3), 287-310.*, 1990a.

R. Pratt. Inverse theory applied to multi-source cross-hole tomography II: Elastic waveequation method. *Geophysical Prospecting, 38, 311–330.*, 1990b.

R. Pratt, F. Hou, K. Bauer, and M. Weber. Waveform tomography images of velocity and inelastic attenuation from the Mallik 2002 Crosshole Seismic Surveys. *Scientific Results from the Mallik 2002 Gas Hydrate Production Research Well Program, Mackenzie Delta, North Territories, Canada, Vol. 585 of Bulletin, pp. 1–14, eds Dallimore, S.R. Collet, T.S., Geological Survey of Canada.*, 2004.

R. G. Pratt. Seismic waveform inversion in the frequency domain, Part 1: Theory and verification in a physical scale model. *Geophysics, 64(3), 888-901.*, 1999.

R. G. Pratt, C. Shin, and G. Hick. Gauss–Newton and full Newton methods in frequency–space seismic waveform inversion. *Geophysical Journal International, 133(2), 341-362.*, 1998.

C. Ravaut, S. Operto, L. Improta, J. Virieux, A. Herrero, and P. Dell'Aversana. Multiscale imaging of complex structures from multifold wide-aperture seismic data by frequency-domain full-waveform tomography: Application to a thrust belt. *Geophysical Journal International, 159(3), 1032-1056.*, 2004.

A. Romdhane, E. Querendez, and C. Ravaut. CO2 Thin-layer Detection at the Sleipner Field with Full Waveform Inversion: Application to Synthetic and Real Data. *Energy Procedia, (51), 281-288.*, 2014.

. B. B. Sava, P. Wave-equation migration velocity analysis. I. Theory. *Geophysical Prospecting, 52(6), 593-606.*, 2004.

R. E. Sheriff and L. P. Geldart. *Exploration seismology*. Cambridge university press, Cambridge, London, 1995.

L. Sirgue and R. Pratt. Efficient waveform inversion and imaging: A strategy for selecting temporal frequencies. *Geophysics, 69(1), 231-248.*, 2004.

Z.-M. Song, P. Williamson, and R. Pratt. Frequency-domain acoustic-wave modeling and inversion of crosshole data. Part II— inversion method, synthetic experiments and real-data results. *Geophysics, 60(3), 796–809.*, 1995.

C. Stork. Re[U+FB02]ection tomography for the postmigrated domain. *Geophysics, 57, 680–692.*, 1992.

A. Tarantola. Inversion of seismic reflection data in the acoustic approximation. *Geophysics, 49(8), 1259-1266.*, 1984.

D. Vigh, S. B., K. J., and L. H. 3D full waveform inversion on a Gulf of Mexico WAZ data set. *Proceedings of the 80th SEG Annual International Meeting.*, 2010.

J. Virieux and S. Operto. An overview of full-waveform inversion in exploration geophysics. *Geophysics, 74(6), WCC1-WCC26.*, 2009.

P. Zweigel, R. Arts, A. E. Lothe, and E. Lindeberg. Reservoir geology of the Utsira Formation at the first industrial-scale underground CO2 storage site (Sleipner area, North Sea). *Geological Society, London, Special Publications, 233(1), 165-180.*, 2004.